

**TITLE**

Are Changes in Atmospheric Circulation Important for Black Carbon Aerosol Impacts on Clouds, Precipitation, and Radiation?

**AUTHORS**

Johnson, BT; Haywood, JM; Hawcroft, MK

**JOURNAL**

Journal of Geophysical Research: Atmospheres

**DEPOSITED IN ORE**

04 December 2019

This version available at

<http://hdl.handle.net/10871/39948>

---

**COPYRIGHT AND REUSE**

Open Research Exeter makes this work available in accordance with publisher policies.

**A NOTE ON VERSIONS**

The version presented here may differ from the published version. If citing, you are advised to consult the published version for pagination, volume/issue and date of publication

# JGR Atmospheres

## RESEARCH ARTICLE

10.1029/2019JD030568

### Key Points:

- Black carbon aerosol alters atmospheric circulation patterns due to strong absorption of solar radiation
- Adjustments in circulation are important in driving regional changes in precipitation, convection and cloud
- Circulation adjustments have little impact on global-mean precipitation and effective radiative forcing

### Supporting Information:

- Supporting Information S1

### Correspondence to:

B. T. Johnson,  
ben.johnson@metoffice.gov.uk

### Citation:

Johnson, B. T., Haywood, J. M., & Hawcroft, M. K. (2019). Are changes in atmospheric circulation important for black carbon aerosol impacts on clouds, precipitation, and radiation? *Journal of Geophysical Research: Atmospheres*, 124, 7930–7950. <https://doi.org/10.1029/2019JD030568>

Received 28 FEB 2019

Accepted 9 JUN 2019

Accepted article online 18 JUN 2019

Published online 22 JUL 2019

## Are Changes in Atmospheric Circulation Important for Black Carbon Aerosol Impacts on Clouds, Precipitation, and Radiation?

B. T. Johnson<sup>1</sup> , J. M. Haywood<sup>1,2</sup> , and M. K. Hawcroft<sup>2,3</sup> 

<sup>1</sup>Met Office Hadley Centre, Exeter, UK, <sup>2</sup>College of Engineering, Mathematics, and Physical Sciences, University of Exeter, Exeter, UK, <sup>3</sup>Centre for Applied Climate Science, University of Southern Queensland, Toowoomba, Queensland, Australia

**Abstract** Black carbon (BC) aerosols strongly absorb solar radiation, but their effective radiative forcing and impacts on regional climate remain highly uncertain owing to strong feedbacks of BC heating on clouds, convection, and precipitation. This study investigates the role of large-scale circulation changes in governing such feedbacks. In the HadGEM3 climate model BC emissions were increased to 10 times present-day values while keeping sea surface temperatures fixed, to assess the rapid adjustments to increased BC absorption. The BC perturbation led to an effective radiative forcing of 2.7 W/m<sup>2</sup> and a 0.13-mm/day reduction in global precipitation. There were also large shifts in the spatial distribution of tropical convection, increased low cloud over oceans, and a weakening and poleward shift of midlatitude storm tracks, especially in the Northern Hemisphere. In a parallel experiment, horizontal winds were nudged toward meteorological reanalyses to deliberately suppress circulation responses while allowing changes to the thermodynamic structure of the atmosphere. Surprisingly, BC had approximately the same impact on global-mean radiation and global precipitation in the nudged experiment, even though regional changes in clouds and convection were not fully captured. The results show that large-scale dynamical responses to BC are important for regional impacts but have a limited role in determining the effective radiative forcing and global-mean climate response. The rapid adjustments of clouds, radiation, and global precipitation were primarily a response to increased radiative absorption and atmospheric stability. This implies that short nudged simulations may be sufficient to assess absorbing aerosol impacts on global-mean radiation and precipitation.

**Plain Language Summary** Black carbon (BC) aerosols are emitted during the combustion of various types of fuel. These soot-like particles absorb solar radiation and therefore exert a warming influence on climate. However, their impact is highly uncertain as localized heating of the atmosphere also alters clouds, convection, and atmospheric circulation. This leads to strong feedbacks and changes in regional precipitation that vary widely among global models. This study investigates how important changes in atmospheric circulation are in explaining such feedbacks by comparing experiments where BC emissions were increased but changes in atmospheric flow were either permitted or deliberately suppressed via nudging. We find that regional changes in precipitation and cloud over the tropics and midlatitude storm tracks are indeed strongly linked to changes in atmospheric circulation, especially vertical motion. However, some of the impacts on regional cloud and precipitation were connected to more basic thermodynamic adjustments in the atmosphere. Moreover, the impact of BC on global-mean radiation and precipitation was approximately the same whether the atmospheric flow was constrained or free to respond and adjust. We conclude that accurately capturing the feedback of BC on atmospheric circulation is essential to predicting regional changes in precipitation but may be less important for global-mean climate impacts.

### 1. Introduction

Black carbon (BC) aerosols strongly absorb solar radiation in the atmosphere and are expected to exert a warming influence on the climate system due to their positive radiative forcing (Bond et al., 2013; Myhre et al., 2013; Ramanathan & Carmichael, 2008; Zhang & Wang, 2011). Due to radiative heating in the atmosphere and reduction of solar radiation at the surface, BC also increases atmospheric stability, leading to reduced global precipitation and strong impacts on cloud cover and convection. The impact of BC on clouds was previously termed the semidirect aerosol effect (Hansen et al., 1997) and was originally proposed as a positive feedback since BC heating was expected to reduce cloud cover, particularly in the boundary layer

(Ackerman et al., 2000; Johnson et al., 2004). Most current general circulation models, however, show that BC induces a net negative feedback due to a broader range of rapid adjustments (RA) in the atmosphere. The term *rapid adjustments* encapsulates feedbacks in the atmosphere and land system that occur in response to the forcing but prior to the more slowly evolving changes in sea surface temperatures (SSTs; Forster et al., 2016). In the case of BC, the dominant RA affecting the radiation budget are reductions in high cloud, increasing outgoing longwave (LW) radiation; increases in low-level stratocumulus, increasing outgoing shortwave (SW) radiation (Koch and Del Genio, 2010; Stjern et al., 2017); and negative LW feedback due to warming of the upper troposphere (Sand et al., 2015; Smith et al., 2018). These adjustments in cloud and temperature are linked to BC increasing the static stability of the troposphere and associated reductions in convection at the global scale (Andrews et al., 2010; Frieler et al., 2011; Ming et al., 2010; Myhre et al., 2018; Samset et al., 2016). However, at regional scales absorbing aerosol can increase or decrease precipitation and convection as atmospheric dynamics adjust to the inhomogeneous distribution of radiative heating (Menon et al., 2002; Meehl et al., 2008; Wang, 2009; Liu et al., 2018). The impacts of BC on convection are complex and highly dependent on its vertical distribution (e.g., Wang, 2013a; Samset & Myhre, 2015). For instance, BC heating in the boundary layer may reduce shallow convection but enhance the buildup of moisture and convective available potential energy for subsequent deep convection (Fan et al., 2015; Lin et al., 2016). The impacts of BC on climate may therefore be felt most keenly at regional scales and may be disproportionate to the global-mean forcing or global-mean temperature response.

Due to the complex nature of such interactions and disagreement among models, the role of BC in anthropogenic climate change remains uncertain and poorly understood (Andreae & Ramanathan, 2013; Boucher et al., 2013; Wang, 2013b). The problem is compounded by difficulties in constraining the emissions, transport, and atmospheric lifetime of BC, leading to large uncertainties in the BC mass concentrations in models (Bond et al., 2013; Boucher et al., 2016). A further source of uncertainty is the high sensitivity of BC absorption to particle properties and mixing state (Jacobson, 2001; Matsui et al., 2018; Peng, 2016; Samset et al., 2018). These uncertainties pose a major challenge when using observations to constrain the BC absorption in global models (Chung et al., 2012; Koch et al., 2009; Sato et al., 2003; Wang et al., 2014, 2016). Differences in the vertical profile of BC also strongly affect radiative forcing uncertainty (Samset et al., 2013; Zarzycki & Bond, 2010). Consequently, there remains a lack of consensus on the magnitude of BC radiative forcing (Myhre et al., 2013). Moreover, due to the strong negative RA, estimates of instantaneous radiative forcing (IRF) have proven an unreliable guide to impacts of increased BC on temperature and precipitation in coupled models (e.g., Baker et al., 2015; Sand et al., 2015; Stjern et al., 2017).

The study by Stjern et al. (2017) examined the climate response of nine global coupled models to increasing present-day BC emissions by a factor of 10. This BC perturbation led to surprisingly weak temperature increases (a multimodel median response of 0.67 K), mainly due to negative RA. The degree of negative RA varied considerably between the models and the effective radiative forcing (ERF) was between 35% and 88% of the magnitude of the IRF (of the five models that had diagnosed IRF). One reason why RA vary between models is that BC can lead to differing responses in clouds. For instance, while most global models show increases in low clouds and decreases in cirrus associated with suppression of convection, both these responses are highly sensitive to the vertical distribution of BC in models (Johnson et al., 2004; Koch & Del Genio, 2010; Samset & Myhre, 2015). Differences in the baseline simulation of clouds and the prescription of subgrid cloud processes may also influence the magnitude of cloud responses to BC in large-scale models (Johnson, 2005). Myhre et al. (2018) and Smith et al. (2018) also showed that LW feedbacks from changes in tropospheric temperature and water vapor were important contributors to BC RA and its uncertainty among models, alongside differing SW and LW cloud feedbacks. Another potential reason for uncertainty in BC RA could be different dynamical feedbacks among models. This factor has not been well investigated, and we do not yet know whether dynamical feedbacks are important in determining RA at the global scale.

While there are many sources of uncertainty in quantifying BC climate impacts, one fundamental difficulty is that the inhomogeneous heating associated with BC has strong influences on moist dynamical processes at local to regional scales. This means that RA are more important for BC than for other more uniform climate forcings (such as greenhouse gases) and explains why RA dominate the global precipitation response from BC (Samset et al., 2016). Many studies have also shown connections between BC absorption and changes in regional circulation and monsoon precipitation (e.g., Lau & Kim, 2006; Meehl et al., 2008; Menon et al.,

2002). For example, BC absorption has also been linked to broader impacts on global circulation, such as an expansion of the tropics (i.e., the Hadley circulation) in the Northern Hemisphere (NH; Kovilakam & Mahajan, 2015), northward shifts in the Intertropical Convergence Zone (Roberts & Jones, 2004; Wang, 2004; Yoshimori & Broccoli, 2008) and poleward displacement of the mid-latitude jets (Allen et al., 2012). Understanding of these regional circulation changes is growing (Wang et al., 2013b) though it remains a challenge to link this back to uncertainties in how BC affects the global radiation budget and hydrological cycle. One question is whether BC-driven changes in circulation are important only at regional scales or whether they play a key role in global-scale fast feedbacks. This question is difficult to assess with conventional aerosol perturbation experiments and is explored in this study using the technique of nudging.

Nudging relaxes the large-scale flow toward a reanalysis so that only minimal changes in large-scale atmospheric flow can occur in parallel simulations. This strategy has been used to gain more robust assessments of aerosol-cloud interactions (ACI; Zhang et al., 2014; Kooperman et al., 2012; Ghan et al., 2016) where feedbacks on the large-scale flow are assumed to be of secondary importance. In the case of BC forcing we expect dynamical feedbacks to be more important and use nudging to deliberately suppress these. By contrasting results from nudged and nonnudged (free-running) experiments, we aim to show how important such dynamical responses are in explaining global and regional changes to clouds, precipitation, and the radiation budget. This study examines how changes in the distribution of convection and cloud cover relate to thermodynamic and dynamic adjustments. We use fixed SST simulations to isolate these RA from slower SST-driven climate feedbacks. A secondary, more pragmatic, aim of the study is to assess how well the ERF of highly absorbing aerosol can be assessed with nudged simulations. One major advantage of using nudging is that it greatly increases signal-to-noise ratio in aerosol perturbation experiments, allowing more robust results from smaller perturbations and/or shorter simulations. While this has proven valuable in assessing indirect aerosol forcing (e.g., Malavelle et al., 2017), it remains unclear whether this approach is valid, or sufficiently accurate, for aerosols such as BC that generate more substantial changes in atmospheric circulation.

Section 2 explains the methods and experimental design. Section 3 compares results from the free-running and nudged experiments, including the analysis of ERFs, cloud changes, precipitation changes, and an analysis of changes to the atmosphere's heat budget. Conclusions are provided in section 4.

## 2. Methods

### 2.1. HadGEM3 Climate Model Configuration

This study uses HadGEM3-GA7.1, an atmosphere-only configuration of the U.K. climate model using the Global Atmosphere 7.1 (GA7.1) science configuration (Mulcahy et al., 2018; Walters et al., 2019). The model has a resolution of N96 ( $1.25^\circ \times 1.875^\circ$ ) and 85 vertical levels. The model physics includes the Global Model for Aerosol Processes (GLOMAP)-mode aerosol scheme (Mann et al., 2010) running using precalculated oxidants. The climatology of oxidants was generated from a previous 20-year simulation that included online gas-phase atmospheric chemistry using the U.K. Chemistry and Aerosol combined tropospheric and stratospheric chemistry scheme (Morgenstern et al., 2009; O'Connor et al., 2014). The simulations were set up to represent present-day climate with greenhouse gas concentrations and aerosol emissions based on the year 2014 using inputs from the sixth Coupled Model Intercomparison Project (CMIP6; Hoesly et al., 2018). SSTs and sea ice were prescribed based on the climatological average for the period 2000–2014 based on data from Reynolds et al. (2007).

The microphysical and chemical processes represented in GLOMAP-mode are fully described in Mann et al. (2010), with updates for HadGEM3-GA7.1 detailed in Mulcahy et al. (2018). The modal aerosol scheme simulates the full life cycle of aerosols including emissions, microphysical and chemical processes, large-scale and convective transport, and deposition via dry and wet deposition. The scheme simulates ACIs including impacts on cloud brightness and cloud lifetime, and represents direct aerosol-radiation interactions (ARI). Semidirect effects are included as BC absorption modifies radiative heating rates in the atmospheric model and therefore the evolution of clouds. In GLOMAP-mode, BC aerosols are emitted as insoluble Aitken-mode particles and are internally mixed with co-emitted organic carbon. These particles can be deposited via dry deposition or impaction scavenging (washout), can coagulate with other soluble particles, or may age via condensation of sulfate and subsequently transfer to the soluble Aitken or

**Table 1**

*List of Simulations Used in This Study* Nudged/free running

	Aerosol interactions	BC <sub>FFBF</sub> emission scaling factor	Purpose
Free	ARI and ACI	1 (control)	Main (free-running) experiment to assess BC impacts
Free	ARI and ACI	10	
Free	ARI	1	Separate RA into ARI and ACI components
Free	ARI	10	
Nudged	ARI and ACI	1	Nudged experiment to assess BC impacts with dynamical responses suppressed
Nudged	ARI and ACI	10	
Nudged	ARI	1	Separate RA into ARI and ACI components for nudged experiment
Nudged	ARI	10	

*Note.* ARI = aerosol-radiation interactions; ACI = aerosol-cloud interactions; BC = black carbon; BC<sub>FFBF</sub> = BC from fossil fuel and biofuel; RA = rapid adjustments.

accumulation mode. In the soluble modes BC is assumed to be internally and homogeneously mixed with other chemical components in that mode, which may include sulfate, sea salt, organic carbon, and water. In this way, BC emissions can affect the concentration, mass, and hygroscopicity of soluble aerosols acting as cloud condensation nuclei (CCN). There is no microphysical link between simulated aerosols and ice nucleation processes. The soluble-mode particles can be lost via dry deposition, impaction scavenging, or nucleation scavenging (rain-out), including in-plume nucleation scavenging by convective precipitation.

The introduction of convective plume scavenging significantly improved the vertical distribution of BC aerosol in HadGEM3 compared to extensive observations from HIPPO (High-Performance Instrumented Airborne Platform for Environmental Research Pole-to-Pole Observations; Kipling et al., 2013). This reduced the lifetime of BC (global mean is around 4–5 days in HadGEM3-GA7, depending on experimental setup) and helped to address an overestimation of BC in the upper troposphere. A full evaluation of BC aerosol properties was conducted by Mollard (2017), and a subsequent update to BC absorption properties for HadGEM-GA7.1 is described and evaluated in Mulcahy et al. (2018).

## 2.2. Experimental Design

This study involves two experiments, one where the atmosphere evolves freely (free running) and one where nudging is applied to relax horizontal winds toward meteorological reanalyses. Each experiment included a pair of simulations with both ARI and ACI and a pair including only ARI (Table 1). In the second pair ACI were disabled by prescribing cloud droplet number concentrations using a simple land/sea climatology (100/cm<sup>3</sup> over ocean, 350/cm<sup>3</sup> over land). Each pair included a simulation with present-day (2014) aerosol emissions and a simulation with BC emissions from fossil fuel and biofuel (BC<sub>FFBF</sub>) set to 10 times present-day values (amounting to 80 Tg/yr). This provides a large perturbation to the radiation budget, comparable to that of doubling CO<sub>2</sub>. Increasing BC<sub>FFBF</sub> emissions by a factor of 10 proved a successful strategy in the Precipitation Driver Response Model Intercomparison Project (Myhre et al., 2017) and in other BC modeling studies where similar or larger scaling factors were employed (Mahajan et al., 2013; Sand et al., 2015; Yoshimori & Broccoli, 2008). We also completed experiments with 1xBC, 2xBC, and 5xBC and found global-mean impacts on cloud cover, radiation, and precipitation scaled linearly with BC emission (as found in Mahajan et al., 2013). However, regional changes were more statistically significant for 10xBC and are therefore presented in this study. All simulations included a 3-month spin-up followed by a further 20 years that were used for the analysis.

In the nudged simulations the large-scale flow in the model is relaxed toward reanalysis data, here the ERA-Interim data set (Dee et al., 2011). Nudging was applied to horizontal winds but not to temperature, to enable thermodynamic adjustments to BC heating. In this study reanalyses from the period 1997–2018 were used as a representative sample of present-day climate. As recommended in Telford et al. (2008), nudging was applied above 1.5 km, to enable low-level winds to adapt more naturally to local surface conditions and the freely evolving boundary layer structure. The *e*-folding time scale was set to 6 hr, as recommended in Telford et al. (2008), as this keeps the large-scale flow in step with the reanalysis but enables small dynamical adjustments that maintain the flow in a balanced state. Because the reanalyses

originate from a different modeling system to HadGEM3, the baseline climate differs somewhat from that in the free-running control simulation. This may have an additional influence on the nature of dynamical responses.

### 2.3. Method for Calculating of Aerosol Radiative Effects

In this study the ERF has been calculated as the change in net radiative flux at the top of the atmosphere (TOP;  $F$ ) between the 10xBC and control simulations (equation (1)), with SSTs, sea ice, and greenhouse gas concentrations held fixed. This follows the general definition of ERF in Forster et al. (2016), except that our control simulations represent present-day climate rather than preindustrial conditions. The IRF (due to direct absorption and scattering by aerosol) was calculated using a double call to the radiation scheme, as in Ghan et al. (2012). First, the aerosol radiative effect was diagnosed as  $(F - F_{\text{clean}})$ , which gives the change in net TOA flux between the main radiation call including aerosol (providing  $F$ ) and a second “clean” call that omits ARI (providing  $F_{\text{clean}}$ ). Then the IRF was calculated as the change in the aerosol radiative effect between the 10xBC and control simulations (equation (2)).

The influence of RA on net TOA radiation was then evaluated as the difference between ERF and IRF (equation (3)). The RA associated with ARI is denoted  $RA_{\text{ARI}}$  and was evaluated in a similar manner to RA, except that it is based on  $ERF_{\text{ARI}}$  and  $IRF_{\text{ARI}}$ , that is, the ERF and IRF values calculated from the ARI-only simulations (equation (4); also see Table 1 for a list of simulations). The  $RA_{\text{ARI}}$  term includes feedbacks of BC absorption on cloud properties (i.e., the semidirect effect) and on atmospheric temperature and humidity and land surface temperature. Note that the cloud droplet number concentrations are idealized in the ARI-only simulation (see section 2.2), which could affect the sensitivity of the clouds to ARI (i.e., the semidirect effect). The RA due to microphysical ACI of BC ( $RA_{\text{ACI}}$ ; i.e., changes in cloud albedo and lifetime) were then evaluated as the residual of  $RA - RA_{\text{ARI}}$  (equation (5)). This assumes that ARI and ACI processes add linearly in the main simulation; any nonlinear interaction between the two is essentially hidden within the diagnosed  $RA_{\text{ACI}}$  term:

$$ERF = F_{10xBC} - F_{\text{control}} \quad (1)$$

$$IRF = (F - F_{\text{clean}})_{10xBC} - (F - F_{\text{clean}})_{\text{control}} \quad (2)$$

$$RA = ERF - IRF \quad (3)$$

$$RA_{\text{ARI}} = ERF_{\text{ARI}} - IRF_{\text{ARI}} \quad (4)$$

$$RA_{\text{ACI}} = RA - RA_{\text{ARI}} \quad (5)$$

## 3. Results

The impacts of the 10xBC perturbation on global-mean radiation, clouds, convection, and precipitation are summarized in Table 2. The uncertainties in global-mean values give the 10–90% confidence interval based on a one-sample Student's  $t$  test with the variance derived from the interannual variability of the BC impact through the 20 years of the experiment. This gives the confidence in diagnosing a clear impact above the noise of chaotic variability in meteorological patterns. This source of uncertainty is much lower in the nudged experiment as the atmospheric flow in each simulation is anchored to the same reanalyses. This aspect of the experimental design also means that the impacts of BC on such variables are generally statistically significant over a greater proportion of the globe than in the free-running experiment. In the following figures, stippling has been used to mark regions where the local change in a variable is not statistically significant at the 80% confidence level. Note the symbol  $\Delta$  denotes the time-mean change in any given variable (i.e., 10xBC – control) and  $\bar{\Delta}$  denotes the global-mean time-mean change.

### 3.1. Aerosol Radiative Effects

The 10xBC perturbation leads to an ERF of  $2.70 \pm 0.07 \text{ W/m}^2$  in the free-running experiment and  $2.77 \pm 0.01 \text{ W/m}^2$  in the nudged experiment (Figures 1a and 1g), with the uncertainty range reflecting the 10–90% confidence interval based on the interannual variability of the diagnosed ERF. The  $0.07\text{-W/m}^2$  difference in ERF between the nudged and free-running experiments is therefore not statistically significant (based on a



**Table 2**  
Changes in Global Multiannual Mean Radiation, Cloud, and Other Related Variables Due to 10xBC in the Free-Running and Nudged Experiments

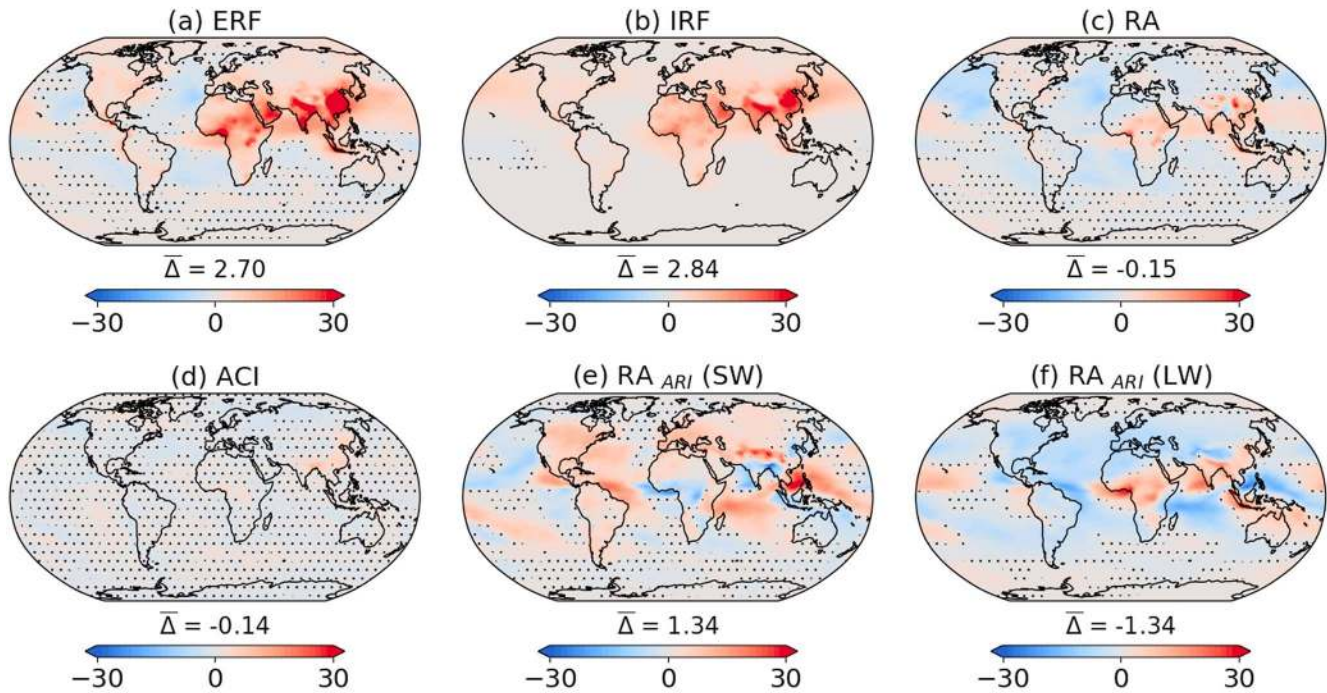
Climate variable/metric	Global-mean free-running control simulation (0xBC)	Global-mean change in the free-running experiment due to 10xBC		Global-mean change in the nudged experiment due to 10XBC	
		Difference with 10–90% uncertainty range	% change relative to control	Difference with 10–90% uncertainty range	% change relative to control
ERF ( $\text{W/m}^2$ )	n/a	$2.70 \pm 0.07$	n/a	$2.77 \pm 0.01$	n/a
IRF ( $\text{W/m}^2$ )	n/a	$2.84 \pm 0.02$	n/a	$2.78 \pm 0.01$	n/a
RA ( $\text{W/m}^2$ )	n/a	$-0.15 \pm 0.07$	n/a	$-0.01 \pm 0.01$	n/a
ACI ( $\text{W/m}^2$ )	n/a	$-0.14 \pm 0.07$	n/a	$-0.11 \pm 0.01$	n/a
ARI adjustments ( $\text{W/m}^2$ )	n/a	$0.00 \pm 0.07$	n/a	$-0.10 \pm 0.02$	n/a
ARI adjustments SW ( $\text{W/m}^2$ )	n/a	$1.34 \pm 0.08$	n/a	$1.26 \pm 0.02$	n/a
ARI adjustments LW ( $\text{W/m}^2$ )	n/a	$-1.34 \pm 0.07$	n/a	$-1.16 \pm 0.01$	n/a
Net absorption in atmosphere ( $\text{W/m}^2$ )	-109.0	$5.62 \pm 0.05$	5.2%	$5.55 \pm 0.03$	7.1%
Net radiation at surface ( $\text{W/m}^2$ )	109.0	$-2.92 \pm 0.04$	2.7%	$-2.78 \pm 0.02$	-2.5%
Surface sensible flux ( $\text{W/m}^2$ )	17.9	$-1.69 \pm 0.03$	-9.5%	$-1.69 \pm 0.02$	-9.5%
Surface latent flux ( $\text{W/m}^2$ )	90.3	$-3.93 \pm 0.07$	-4.3%	$-3.85 \pm 0.03$	-4.2%
Precipitation (mm/day)	3.12	$-0.136 \pm 0.002$	-4.3%	$-0.133 \pm 0.001$	-4.3%
Associated latent heat ( $\text{W/m}^2$ )	90.3	$-3.93 \pm 0.07$		$-3.85 \pm 0.03$	
Column-max convective mass flux (Pa/s)	0.0593	$-0.0039 \pm 0.0001$	-6.6%	$-0.0044 \pm 4e-5$	-7.4%
Low cloud fraction (%)	32.9	$0.50 \pm 0.05$	1.5%	$0.53 \pm 0.01$	1.6%
Middle cloud fraction (%)	16.6	$-0.76 \pm 0.02$	-4.6%	$-0.74 \pm 0.01$	-4.5%
High cloud fraction (%)	36.0	$-1.04 \pm 0.06$ (-2.8%)		$-0.08 \pm 0.02$ (-0.2%)	
Total cloud fraction (%)	63.6	$-0.69 \pm 0.07$ (-1.1%)		$0.23 \pm 0.02$ (0.4%)	
LWP ( $\text{g/m}^2$ )	47.9	$-0.42 \pm 0.10$ (-0.9%)		$-0.49 \pm 0.01$ (1.0%)	
IWP ( $\text{g/m}^2$ )	49.9	$-1.99 \pm 0.09$ (-4.0%)		$-1.36 \pm 0.02$ (-2.7%)	

Note. ERF = effective radiative forcing; IRF = instantaneous radiative forcing; RA = rapid adjustments; ACI = aerosol-cloud interactions; ARI = aerosol-radiation interactions; LWP = liquid water path; IWP = ice water path; n/a = not applicable.

Student's *t* test at the 80% confidence level). The parity in results between the nudged and free-running experiments is somewhat surprising, given the conceptual difference in experimental design. In both experiments the ERF is dominated by the IRF (Figures 1b and 1h), which has almost the same global-mean value as the ERF. For reference, the BC aerosol absorption optical depth from the free-running control and 10xBC simulations are shown in Figure S1. This highlights the impact of the 10xBC perturbation on column-integrated absorption and predominantly explains the distribution of IRF shown in Figures 1b and 1d. To put the 10xBC results into context, the preindustrial to present-day BC ERF for this model is  $0.30 \text{ W/m}^2$  based on the 1850–2014 CMIP6 emissions or  $0.17 \text{ W/m}^2$  based on the CMIP5 1850–2000 emissions. The corresponding IRF estimates were  $0.41$  and  $0.21 \text{ W/m}^2$ , respectively. These estimates fit well within the range of BC ERF and IRF estimates from the recent assessments of Myhre et al. (2013) and Bond et al. (2013). More detailed information and discussion of the historical BC forcing is provided in the supporting information and Table S1.

Surprisingly, in this model the RA lead to almost no change in global-mean net radiation at the TOA (the RA term was  $-0.15 \pm 0.07 \text{ W/m}^2$  in the free-running experiment and  $-0.01 \pm 0.01 \text{ W/m}^2$  in the nudged experiment). On regional scales there are strong and statistically significant negative and positive RA of up to  $\pm 15 \text{ W/m}^2$  in magnitude (Figures 1c and 1i). For instance, the RA term is negative over many subtropical ocean regions but positive over tropical Africa and Asia. These regional-scale adjustments to TOA radiation mainly originate from feedbacks associated with ARI (i.e.,  $\text{RA}_{\text{ARI}}$ ; Figures 1e–1f and 1k–1l). These lead to strong changes in outgoing SW and LW radiation that approximately cancel one another globally, though not regionally. The spatial patterns are broadly similar in the nudged and free-running experiments though the nudging seems to favor stronger local changes in the tropics and weaker changes over the subtropics and midlatitudes. These strong heterogeneous region patterns predominantly relate to changes in cloud cover, as explored in the next section. Changes in atmospheric temperature, humidity, surface temperature, and albedo also contribute but to a lesser extent, as indicated by the comparatively weak ARI adjustments to clear-sky radiation (Figure S2). As shown by Smith et al. (2018), RA from changes in atmospheric

## Free-running



## Nudged

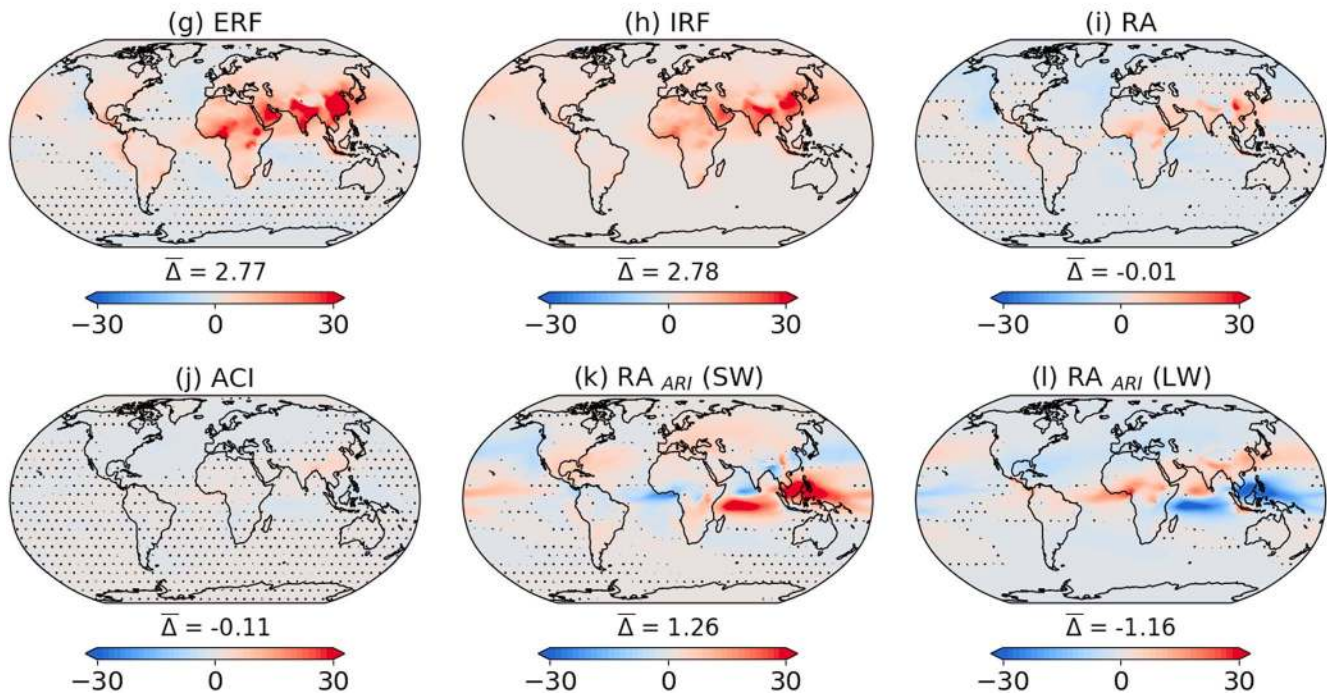


**Figure 1.** Impacts of 10xBC on top of atmosphere radiation balance ( $\text{W/m}^2$ ) for the free-running and nudged experiments: (a, g) Effective radiative forcing (ERF), (b, h) instantaneous radiative forcing (IRF), (c, i) rapid adjustments (RA), (d, j) aerosol-cloud interactions (ACI; microphysical), and (e-f, k-l) rapid adjustments associated with the aerosol-radiation interactions (ARI), segregated into shortwave (SW) and longwave (LW) components. Stipples indicate regions where changes are not statistically significant at the 80% confidence level. (top two rows) From the free-running experiment and (bottom two rows) from the nudged experiment.



temperature and humidity changes can be relatively strong for BC, but their impact on TOA radiation may cancel, which is the case in our model experiments.

In these simulations BC leads to weak negative ACI adjustments (free:  $-0.14 \pm 0.07 \text{ W/m}^2$ , nudged:  $0.11 \pm 0.01 \text{ W/m}^2$ ) that are only significant over limited regions (Figures 1d and 1j). Scaling up BC emissions in our model increases the number concentration of insoluble Aitken-mode particles, and many of these subsequently age into soluble particles (via condensation of  $\text{H}_2\text{SO}_4$ ), generally increasing the concentration of CCN. However, in some polluted regions (e.g., Asia) very large increases in BC particle emissions actually reduced the effective number of CCN. This is because fresh BC particles act as a sink for the limited supply of aerosol precursor gases, and this can limit nucleation, ageing, and the growth rate of existing soluble particles. As found in some other models, these competing factors may reduce the concentration of particles developing into viable CCN (Koch et al., 2011). Nudging the winds does not appear to alter the magnitude or spatial characteristics of the ACI response but does improve the statistical significance of the results by limiting the influence of meteorological variability. This greatly reduces the uncertainty in global-mean estimates of radiative impacts and also increases the global area where statistically significant radiative impacts can be diagnosed. This is true for all components in Figure 1 but particularly aids the diagnosis of the relatively weak ACI term. This corroborates previous studies showing nudging to be a suitable and computationally efficient framework for quantifying ACI in global models (Ghan et al., 2016; Kooperman et al., 2012; Zhang et al., 2014).

In summary, BC RA have virtually no impact on global-mean TOA net radiation in HadGEM3-GA7.1, for either experiment. This result is uncharacteristic, since many other modeling studies have shown RA to be overall negative for BC and to diminish the ERF of BC to substantially less than the IRF (e.g., Mahajan et al., 2013; Sand et al., 2015; Stjern et al., 2017). Further analysis is necessary to understand why this is not the case for our model. Perhaps difficulties associated with modeling clouds in large-scale models (e.g., Johnson et al., 2005) still frustrate drawing concrete conclusions.

### 3.2. Impacts on Cloud and Precipitation

Figure 2 shows the impacts of BC on large-scale cloud properties and related changes in precipitation and lower tropospheric stability (LTS).

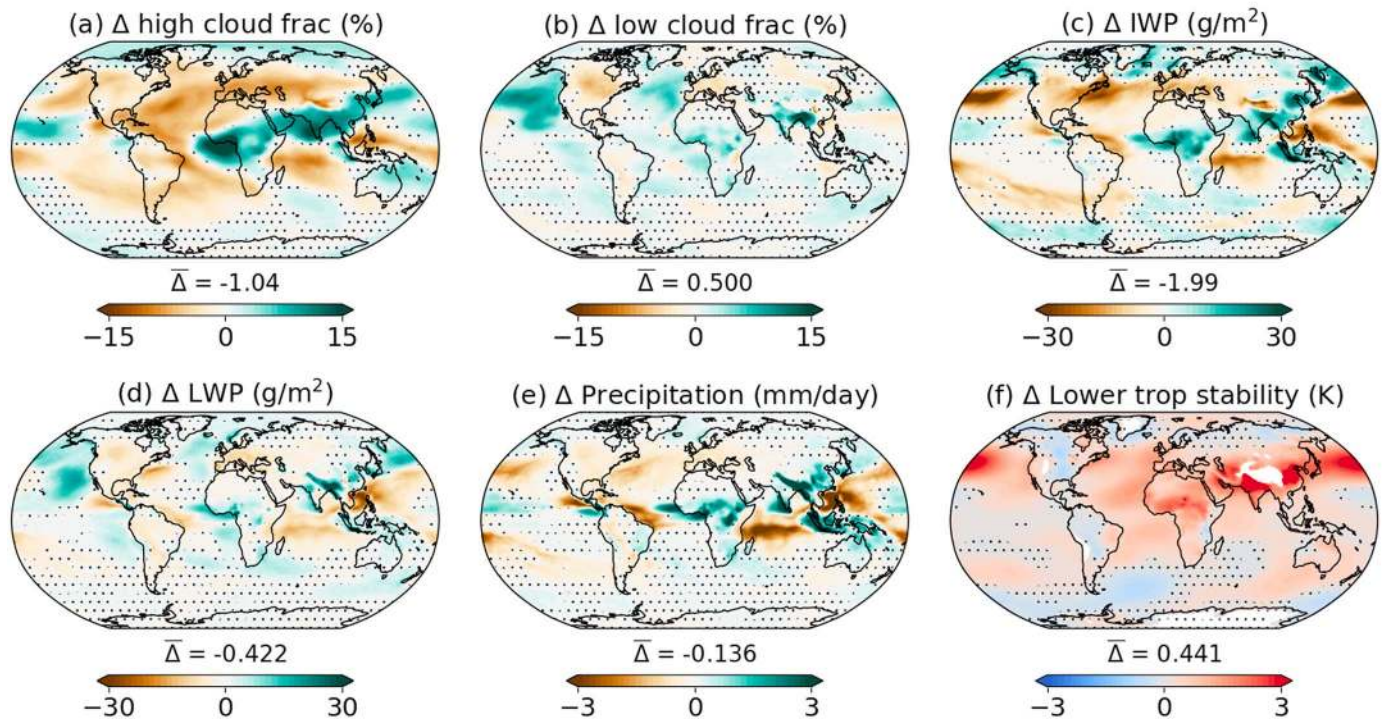
#### 3.2.1. High Clouds

As found in earlier global modeling studies (e.g., Koch & Del Genio, 2010; Stjern et al., 2017), we find that BC absorption leads to an overall reduction of high cloud (Figures 2a and 2g) and ice water path (IWP; Figures 2c and 2i) due to the suppression of deep convection. There are also statistically significant regional changes including increases of high cloud, IWP, and liquid water path (LWP) in a belt stretching over tropical Africa and Asia. High cloud fraction and IWP are reduced over most midlatitudes zones, particularly in the NH, and across many other parts of the tropics. The nudged experiment captures most of the high cloud changes in the tropics (Figure 2c), except for those over South America and the Tropical West Atlantic, and has much weaker changes in the midlatitudes. In the tropics, high cloud is mainly produced by detrainment from deep precipitating convective systems and spreads out laterally due to divergence in the upper troposphere. This explains why the changes in high cloud fraction and IWP are broadly consistent with regional-scale changes in precipitation (Figures 2e and 2k). The patterns of LW radiation adjustments ( $\text{RA}_{\text{ARI}}$ ) shown in Figures 1f and 1l are also consistent with the changes in high cloud and IWP, since high-altitude cirrus cloud is effective at reducing outgoing LW radiation. The changes in IWP correlate best with the LW  $\text{RA}_{\text{ARI}}$  term in the tropics, particularly in the nudged experiment (linear regression  $R^2 = 0.81$ ; see Table S2). The changes in cloud are statistically significant over a greater proportion of the globe in the nudged experiment as nudging reduces the uncertainty associated with chaotic variability in atmospheric flow.

#### 3.2.2. Precipitation

BC absorption reduces global precipitation by  $0.136 \pm 0.002 \text{ mm/day}$  in the free-running experiment and  $0.133 \pm 0.001 \text{ mm/day}$  in the nudged experiment (Table 2 and Figures 2e and 2k). This matches the reduction in the surface latent heat flux associated with evaporation (Table 2) and is consistent with the stabilizing influence of BC on the atmosphere. The reductions in global precipitation are also consistent with the requirement to rebalance the atmosphere's heat budget (e.g., Myhre et al., 2018; Richardson et al., 2018), which is explored later in section 3.4. The global-mean and local changes in precipitation are almost

## Free-running



## Nudged

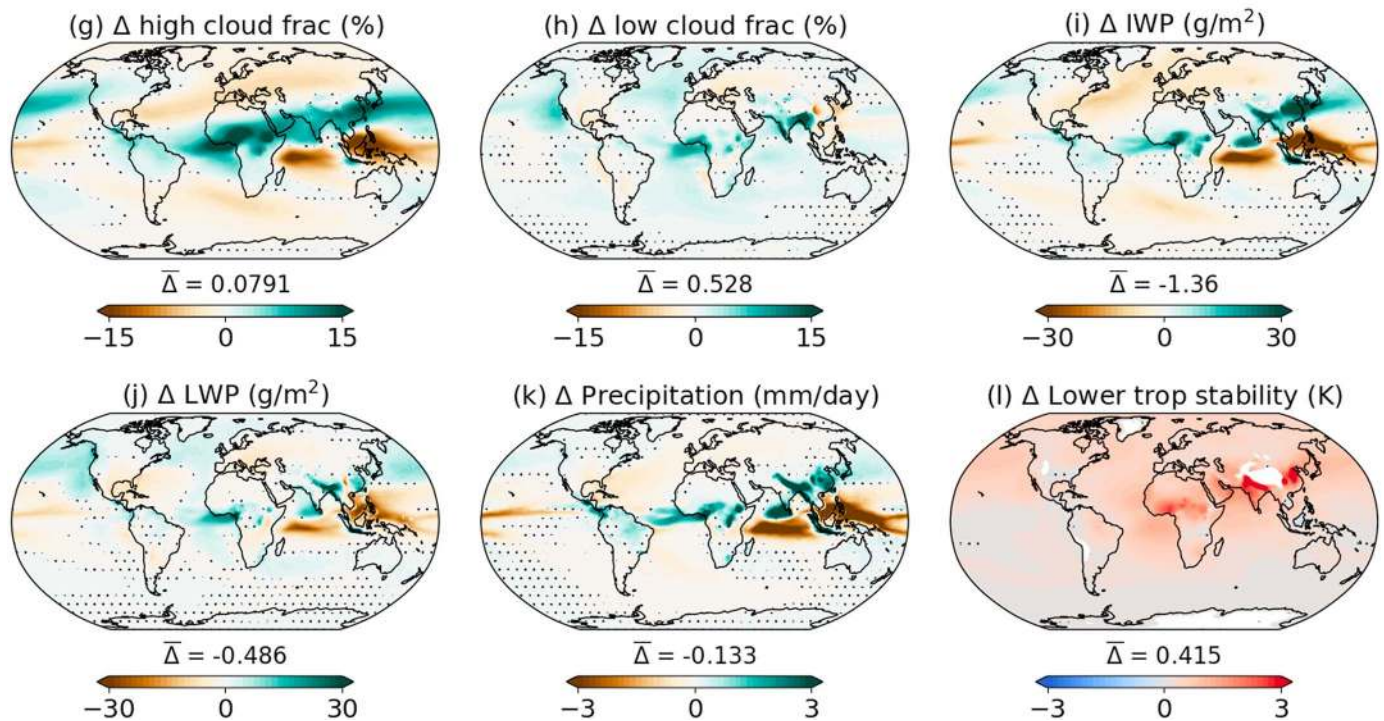


**Figure 2.** Impacts of black carbon on multiannual mean cloud, precipitation, and associated variables in the (top two rows) free-running and (bottom two rows) nudged experiments. Variables include (a, g) high cloud fraction, (b, h) low cloud fraction, (c, i) ice water path (IWP), (d, j) liquid water path (LWP), (e, k) precipitation, (f, l) lower tropospheric stability ( $\theta_{700\text{mb}} - \theta_{\text{sfc}}$ ). Stipples indicate regions where changes are not statistically significant at the 80% confidence level.

entirely due to changes in convective (parameterized) precipitation, with weak or mostly insignificant changes in stratiform precipitation (Figure S5). This is not a complete surprise as convective precipitation accounts for just over 70% of global precipitation in the control climate and almost all precipitation in the tropics (Figure S5). The model's response is therefore understandable, but it should be noted that the high proportion of convective precipitation in this model, and many other models, does not necessarily agree with observations (e.g., Dai, 2006).

BC also leads to statistically significant increases and decreases in regional precipitation due to changes in the spatial distribution of deep convection (Figures S5e and S5k). Local enhancements in precipitation are greatest in the tropics and reach 2–4 mm/day (750–1,500 mm/year) over parts of Tropical Asia and Tropical Africa. The greatest reductions of –2 to –4 mm/day occur over the Indian Ocean and tropical West Pacific. The enhancements to precipitation over Tropical Asia and Africa also occur where BC radiative heating is strong, as indicated by the large TOA IRF in Figures 1b and 1h, and where annual precipitation is already high (Figures S5a and S5g). The greatest suppression of precipitation occurs in adjacent regions where BC heating is weak or close to zero, but annual precipitation is high in the control simulation. The changes in precipitation correlate very strongly with local changes in convective mass flux and vertical velocity, especially in the tropics (Table S2). Significant shifts in the distribution of tropical convection have been shown in previous modeling studies that perturb global emissions of BC (e.g., Sand et al., 2015; Stjern et al., 2017; Wang, 2009). As discussed in the aforementioned studies, this indicates some feedback between BC heating, vertical motion, and latent heat release via convection. The result here also echoes the findings of Chadwick et al. (2013) where strong regional changes in tropical precipitation due to CO<sub>2</sub> forcing were explained via adjustments to the baseline thermodynamic state of the atmosphere and the modulation of preexisting circulations. The free-running experiment also shows statistically significant reductions in precipitation in the NH storm tracks, North America, and central to southern Europe, which are broadly consistent with findings from previous studies (e.g., Tang et al., 2018; Yoshimori & Broccoli, 2008). The regional precipitation changes in the nudged experiment are similar to those in the free-running experiment, except that changes in midlatitudes are weaker with the nudging. Precipitation responses to BC in the extratropics are therefore strongly connected to changes in large-scale circulation that the nudging has suppressed. The reductions of precipitation in the Indian Ocean and tropical West Pacific also appear stronger in the nudged experiment. One reason for this is that the nudging only allows small changes in flow so that the adjustments in circulation are more confined to the region around the BC forcing. Another factor could be differences in the baseline climate in the nudged and free-running simulations. For instance, the spatial distributions of annual mean precipitation in the Eastern Tropics (30°S–30°N, 0–180°E) are slightly different in the nudged and free-running control simulations (Figures S5a and S5g), and this may affect the spatial pattern and magnitude of the BC response at local to regional scales.

### 3.2.3. Low Clouds Over Ocean and Tropospheric Stability

Low cloud fraction (Figures 2b and 2h) and LWP (Figures 2d and 2j) generally increase over oceans, especially in the NH. The strongest increases, of up to 15%, are in the Northeast Pacific in the free-running experiment. This tendency to thicken low cloud is consistent with BC heating leading to increased LTS (Figures 2f and 2l), which favors the formation of marine stratocumulus (Johnson et al., 2004; Koch & Del Genio, 2010; Stjern et al., 2017; Wilcox, 2010). This response is in essence captured in the nudged experiment, although the changes in low cloud fraction and LWP are less pronounced over the North Pacific and North Atlantic (Figures 2b, 2d, 2h, and 2j), related to weaker or more globally uniform increases in LTS (Figures 2f and 2l). The increased low cloud fraction and LWP over the marine stratocumulus regions most likely explain the negative ARI adjustments ( $RA_{ARI}$ ) in the SW radiation budget over the Northeast Pacific, Northeast Atlantic, Southeast Pacific, and Southeast Atlantic (Figures 1e and 1k). Indeed,  $RA_{ARI}$  (SW) correlates well with  $\Delta LWP$ ,  $\Delta$ total water path, and  $\Delta$ total cloud fraction, even at the global scale (Table S2).

### 3.2.4. Low Cloud Over Continents

Low cloud changes over the continents vary, but there are strong decreases (of up to 10%) over North America, Europe, and parts of Asia. As land surface temperatures are free to respond in these experiments, BC heating does not necessarily lead to increased LTS over continental regions (Figures 2f and 2l). Instead, the combination of BC warming and drying associated with decreased precipitation (Figures 2e and 2k) leads to reduced low-level relative humidity and cloud cover over many land areas in the NH (Figure S3).



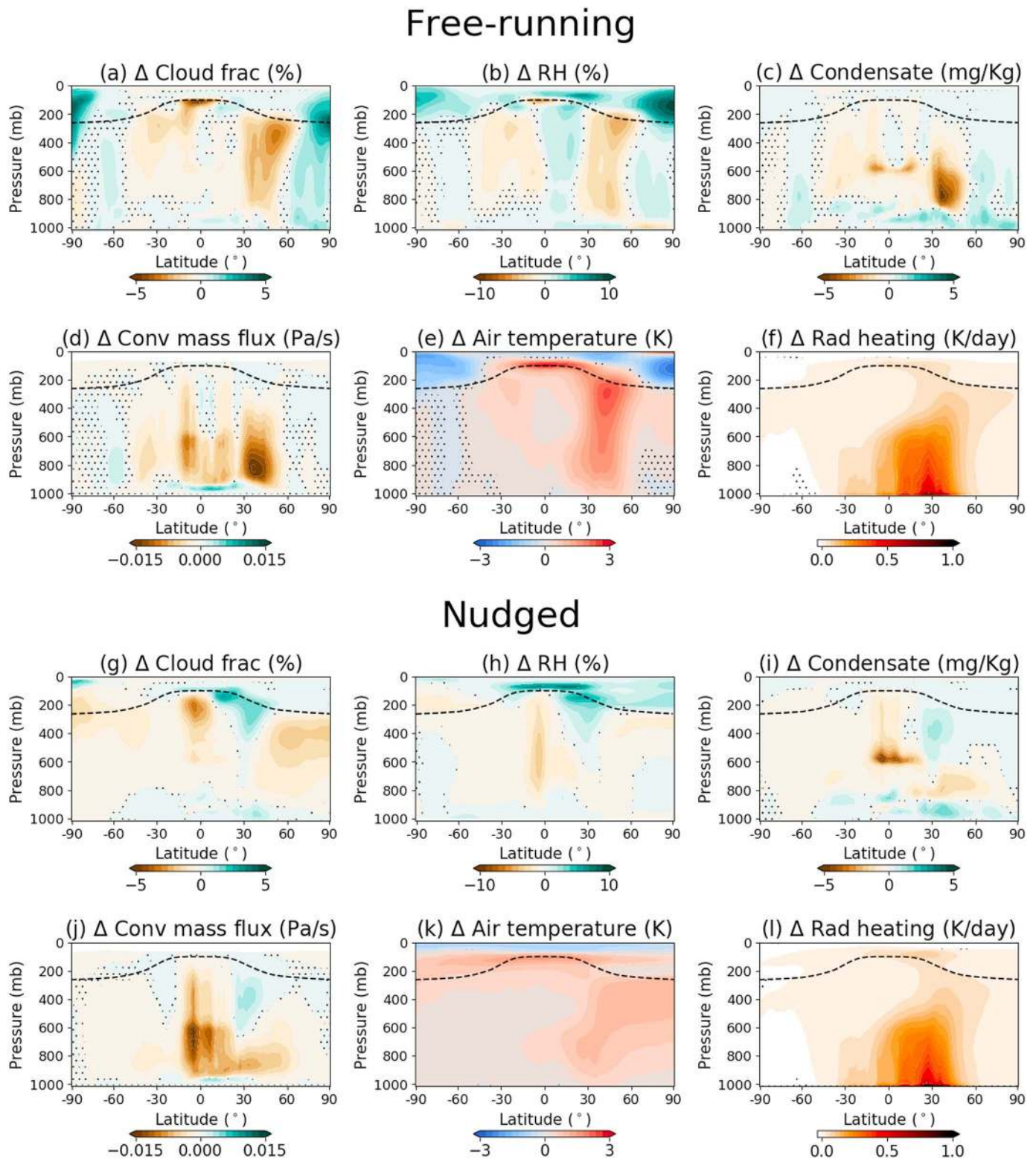


**Figure 3.** Impacts of 10xBC on zonal-mean multiannual mean cloud and thermodynamic variables from the (top two rows) free-running and (bottom two rows) nudged experiments. Variables include (a, g) stratiform cloud fraction, (b, h) relative humidity (RH), (c, g) total cloud condensate (liquid + ice), (d, j) convective mass flux summed from shallow, midlevel, and deep convection parameterizations, (e, k) air temperature, (f, l) net radiative heating rate due to black carbon increases and rapid adjustments. Dashed line indicates multiannual mean height of tropopause, and stipples mask regions where changes are not statistically significant at the 80% confidence level.



Although this simple “cloud burn-off” mechanism does not dominate the low-cloud response to BC globally (as originally proposed by Hansen et al., 1997), it clearly has a role in some continental regions. As in Allen and Sherwood (2010), the impacts are larger in the summer season (not shown). The response is much weaker in the nudged experiment (Figures S3e–S3h), showing that the warming and drying is not simply a local response to BC heating. Changes in larger-scale atmospheric circulation also evidently contribute to, or augment, this response. The associated reductions in low cloud fraction and LWP contribute to the positive SW ARI adjustments ( $RA_{\text{ARI}}^{\text{SW}}$ ) over NH continents (Figures 1e and 1k), accompanied by decreases in high cloud fraction and IWP.

### 3.2.5. Changes in Zonal-Mean Cloud and Moist Thermodynamic Variables

Figure 3 further illustrates the impacts of BC on clouds by showing changes in annual-mean zonal-mean cloud properties and related thermodynamic variables. The pattern of radiative heating change is almost identical in the free-running and nudged experiments (Figures 3f and 3l), but the patterns of changes in temperature (Figures 3e and 3k) and other variables (Figures 3a–3d and 3g–3j) are considerably different.

The free-running experiment shows large statistically significant reductions of cloud fraction (Figure 3a) and cloud condensate (Figure 3c) in the NH midlatitudes (30–60°N), indicating a likely reduction in frontal cloud. These correspond to a 2–5% reduction in relative humidity (Figure 3b) and 2–3 K increase in temperature from 800 to 200 mb around 40–50°N (Figure 3e). The convective mass flux and cloud condensate also reduce in the NH midlatitudes from 850 to 350 mb (Figures 3d and 3c), which is indicative of suppressed deep convection and reduced frontal activity, as the model’s midlevel convection scheme typically triggers around frontal zones. The zonal-mean analysis also highlights the overall decrease in deep convective mass flux across the tropics (Figure 3d), and the corresponding decrease in relative humidity (Figure 3b) and high-altitude cirrus (Figure 3a) in the tropical upper troposphere (150–200 mb), plus a warming of up to 3 K around the tropopause (150 mb; Figure 3e).

The pattern of zonal-mean temperature change (Figure 3e) does not directly match the change in zonal-mean radiative heating (Figure 3f), indicating that thermodynamic adjustments and changes in circulation largely explain the changes in thermal structure, relative humidity, and cloud. The spatial pattern of zonal-mean temperature change is very consistent with those shown in other coupled model experiments (Kovilakam & Mahajan, 2015; Sand et al., 2015; Yoshimori & Broccoli, 2008). The transport of heat into the NH midlatitude upper troposphere therefore appears to be a consistent dynamical adjustment in global models.

In the nudged experiment, changes in zonal-mean cloud fraction and condensate are considerably different (Figures 3g–3l). There is a much weaker indication of reduced frontal cloud across the NH extratropics between 40°N and 90°N, but there are stronger reductions in condensate and convective mass flux (Figures 3i and 3j) in the tropics. The pattern of changes in zonal-mean temperature is also much smoother. These differences in results indicate that large-scale dynamical feedbacks play a major role in how the thermodynamic structure of the atmosphere adjusts to BC heating.

## 3.3. Dynamical Adjustments

### 3.3.1. Changes in Vertical Motion

Figures 4a and 4b show the changes in multiannual mean vertical velocity at 500 mb in the two experiments. In the free-running experiment there are strong statistically significant increases in ascent in a belt from the Tropical East Atlantic through Africa and Tropical Asia. Compensating descent (or decreased ascent) occurs elsewhere in tropics especially the Indian Ocean and West Pacific. There are also negative changes in vertical velocity in the NH midlatitudes, especially the Northeast Pacific and across the North Atlantic storm track into Europe. Vertical ascent, convective mass flux, and precipitation are all physically linked and highly correlated, especially in the tropics (Table S2). Note the parameterized convective mass flux does not imply an additional source of gridbox-mean ascent as the upward mass flux is assumed to be balanced by downdraughts and more gradual descent elsewhere within that gridbox.

The nudged experiment shows similar patterns of vertical velocity changes (Figure 4b) in the tropics, with strong increases over Tropical Africa and Asia and decreases in vertical motion in the Indian Ocean and West Pacific. The changes in those regions are in fact more exaggerated in the nudged experiment, but

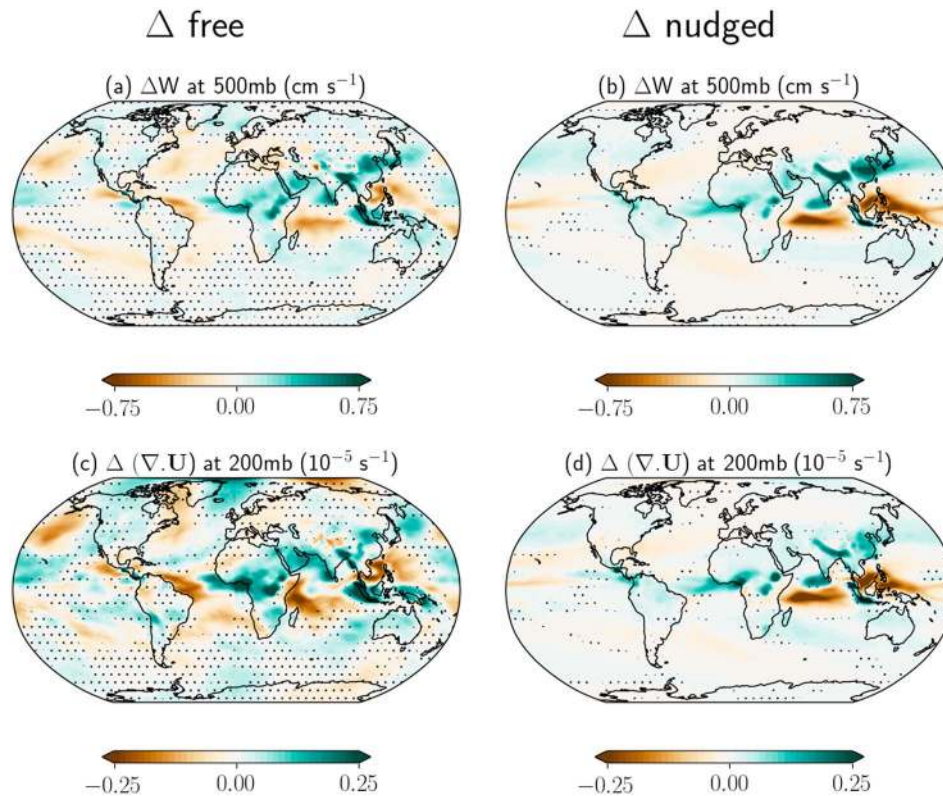


**Figure 4.** Impacts of 10xBC on (a, b) multiannual mean vertical velocity at 500 mb and (c, d) divergence of the horizontal wind flow at 250 mb for the (left column) free-running and (right column) nudged experiments. Stipples indicate regions where changes are not statistically significant at the 80% confidence level.

changes elsewhere in the tropics and in the midlatitudes are weaker. The sign of change reverses to a weak increase in the North Pacific. These results indicate that nudging restricts some dynamical adjustments, particularly those in midlatitudes, but permits changes in circulation in the tropics. To preserve mass continuity, the vertical velocity field must remain consistent with the divergent/convergent component of the horizontal flow (Figure 4d). Indeed, Figures 4c and 4d show that the changes in vertical velocity at 500 mb are coherent with changes in divergence at 200 mb. One might therefore expect nudging the horizontal winds to suppress changes in vertical motion. However, local- to regional-scale changes in vertical motion do still occur in the tropics. Here adjustments to the relatively slow thermally direct circulations require only small deviations ( $\sim 1$  m/s) in  $u$  and  $v$  away from the reanalysis, and these are able to develop despite nudging. Reducing the nudging relaxation time scale from 6 to 3 hr did suppress changes in vertical velocity by around 30–40% in the tropics, but the connection between diabatic heating and vertical motion was still essentially retained.

### 3.3.2. Adjustments to Zonal-Mean Large-Scale Flow

BC heating leads to some interesting shifts in the general atmospheric circulation of the atmosphere, as revealed by the changes in zonal-mean wind shown in Figure 5. The changes in  $u$ ,  $v$ , and  $w$  wind components are statistically significant in most regions but differ quite markedly between the free-running and nudged experiments.

In the free-running experiment the changes in zonal-mean vertical velocity and meridional flow (Figures 5b and 5h) are indicative of a northward shift of the Intertropical Convergence Zone and the associated Hadley cells. This is signaled by the increase in vertical velocity ( $w$ ) at  $20^\circ\text{N}$  and by the decreases in  $w$  across  $10^\circ\text{S}$ – $10^\circ\text{N}$ . There is also decreased  $w$  around  $50^\circ\text{N}$ , indicating an expansion of the subtropics descent zones into the NH midlatitudes, and increases in  $w$  at  $60$ – $70^\circ\text{N}$ , indicating a related poleward displacement of the upward branch of the Ferrell cell. The decrease in  $w$  around  $50^\circ\text{N}$ , associated with these circulation changes, explains the large decrease in relative humidity and increase in temperature in this latitude zone (Figures 3b and 3i).

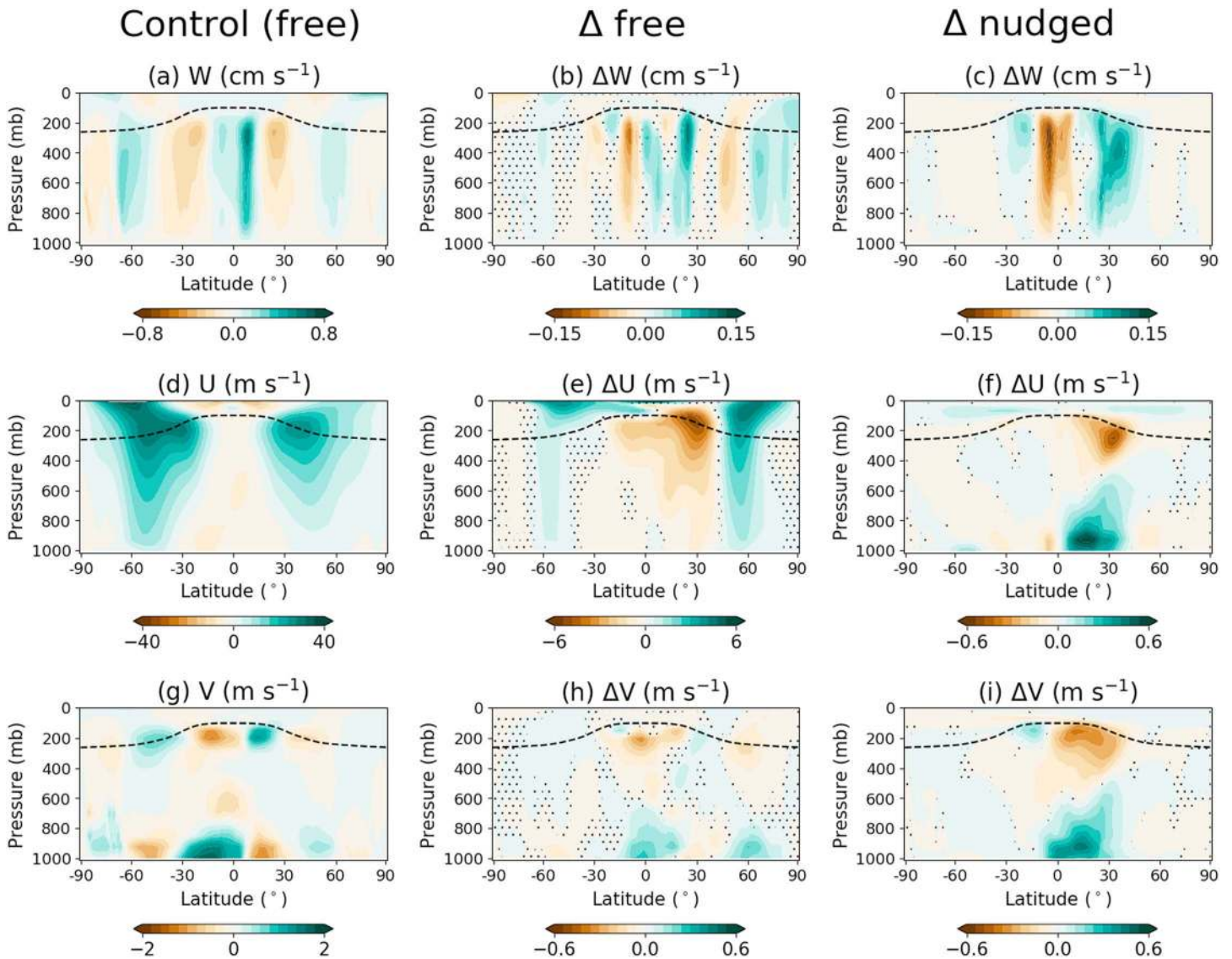


**Figure 5.** Impact of 10xBC on multiannual mean zonal mean wind components, including vertical velocity ( $W$ ), zonal wind component ( $U$ ), and meridional wind component ( $V$ ). Plots show data from the (left) control simulation and the impact of 10xBC in the (middle) free-running and (right) nudged experiments. Stipples indicate regions where changes are not statistically significant at the 80% confidence level.

The free-running experiment also indicates a northward shift in the upper-level jet in the NH midlatitudes, indicated by increases in zonal wind ( $U$  component) on the poleward side of the jet (45–70°N) and decreases on the equatorward side (20–40°N). This is consistent with the temperature change pattern in Figure 3i, which implies a lower meridional temperature gradient on the southern side of the jet (20–40°N) and stronger gradients on the northern side 50–70°N. There is also a slight poleward shift of the subtropical jet in the Southern Hemisphere, along with consistent changes in zonal-mean temperature gradients. The changes in the position of the NH jets were largest during summer (not shown), implicating the role of BC absorption in shifting the midlatitude circulations poleward.

The changes in the nudged experiment are totally different and resemble a single large cell with ascent across 20–50°N and descent across 15°S–10°N. This could be a thermally direct circulation responding to the peak in BC heating across 20–40°N (Figure 3l). This circulation adjustment leads to stronger changes in meridional winds than those in the free-running experiment. However, the changes in zonal flow are an order of magnitude smaller than those in the free-running experiment and do not reflect any poleward shift in the upper-level jets.



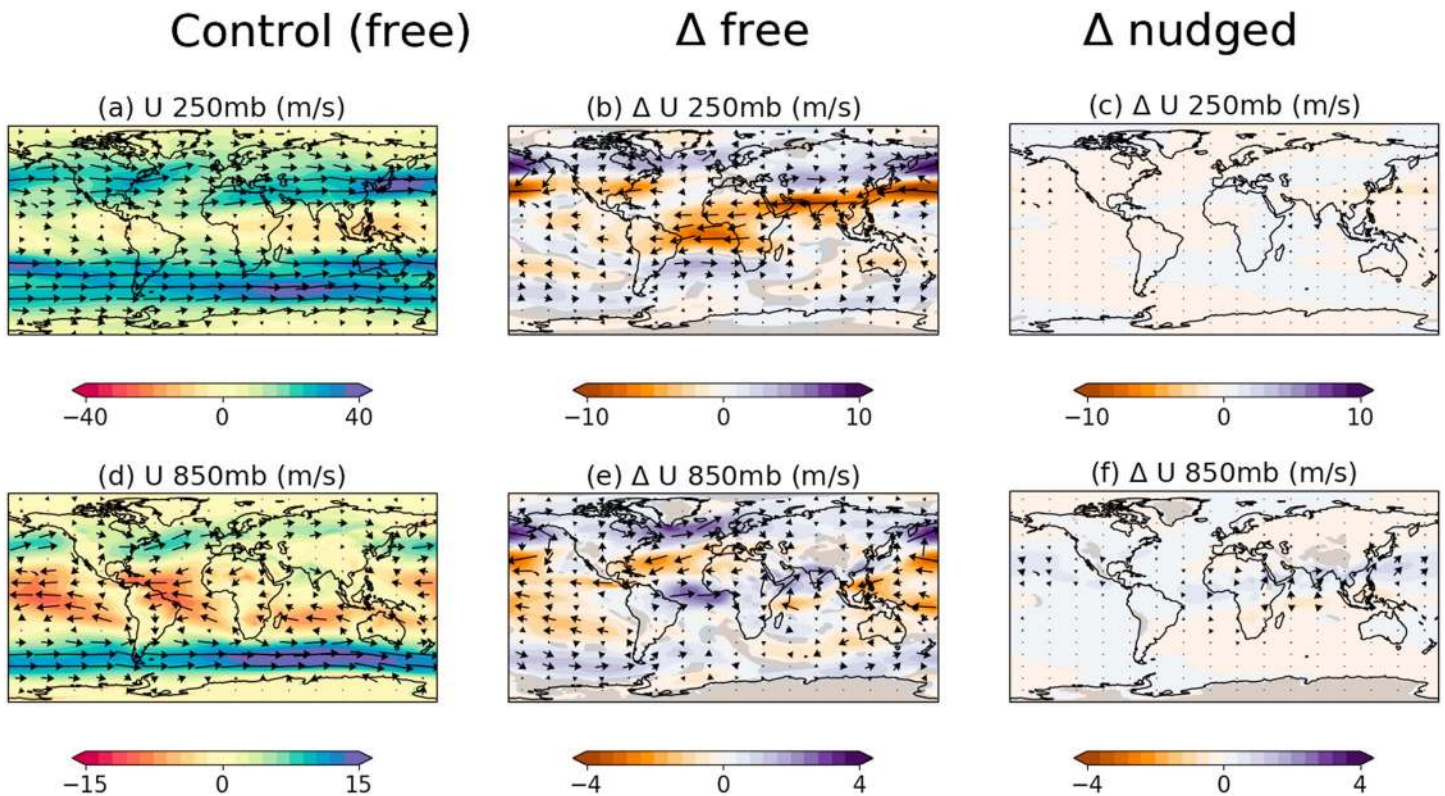


**Figure 6.** Impacts of 10xBC on multiannual mean horizontal winds at (top row) 250 mb and (bottom) 850 mb. Colors indicate the wind velocity in the zonal direction ( $U$ ), and wind vectors show the speed and direction of mean horizontal wind. Plots show values from the (left) control simulation and the impact of 10xBC in the (middle) free-running and (right) nudged experiments. Gray indicates where wind changes were not statistically significant at the 80% confidence level or where 850-mb data are missing due to orography.

### 3.3.3. Changes in Large-Scale Flow

Figure 6 shows the spatial distribution of changes in wind flow at 850 and 250 mb. Once again, there are significant changes in flow patterns in the free-running experiment but much more subdued responses in the nudged experiment. For the free-running experiment, the biggest decreases in 250-mb flow (Figure 6a) are across subtropical Asia and the North Pacific. This may relate to the strong BC absorption in the Asian region (indicated by strong positive TOA forcing in Figure 1a). This is accompanied by increases in atmospheric thickness and 250-mb geopotential height over subtropical Asia and the subtropical North Pacific (Figures S4c and S4e). Over the Tropical Atlantic there is also a strong easterly change in the flow at 250 mb and a westerly change at 850 mb, consistent with weakening of the Atlantic Walker circulation. This corresponds with the reduction in precipitation on the western side of the Tropical Atlantic and increased precipitation over Africa (Figure 2i). Aside from this, the most significant changes in low-level winds correspond to a weakening and poleward shift of low-level westerlies associated with the midlatitude storm tracks, especially across the North Pacific and North Atlantic and to a less extent the Southern Ocean. This weakening and/or poleward shift of surface winds correspond with reduced ascent and precipitation in these storm track regions (Figures 4a and 2i) and increased surface pressure (Figure S4a).

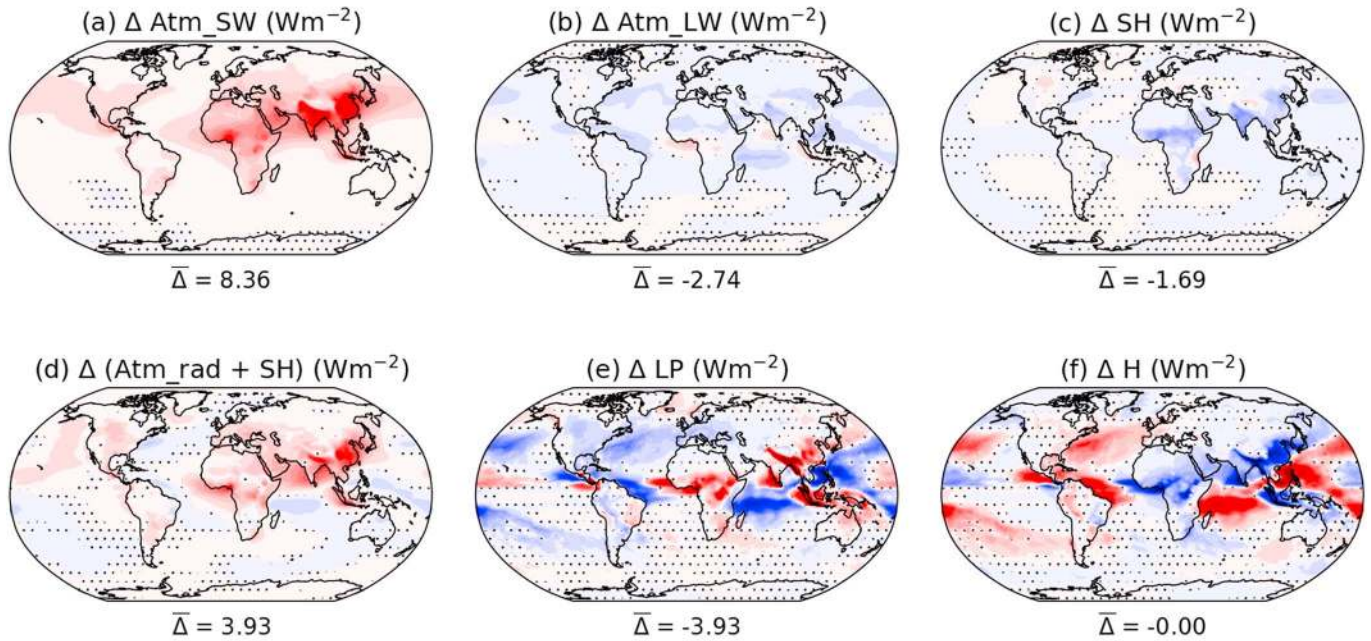
The nudging prevents large changes to the mean flow from developing (Figures 6e and 6f). Since the model's pressure and geopotential height fields must also be consistent with the flow, large regional perturbations in these fields do not develop either (Figures S4b and S4d). The responses that do develop are small adjustments to broad overturning circulations that involve smaller velocities. Midlatitude dynamics involving large eddies and strong jets (i.e., large wind speeds that change rapidly with time) are constrained to follow the reanalysis.

### 3.4. Atmospheric Energy Budget Changes

The energy budget of the global atmosphere involves a balance between net radiative cooling, and heating from surface sensible heat fluxes (SH) and the release of latent heat associated with precipitation (LP).



## Free-running



## Nudged

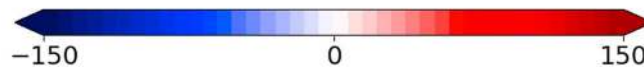
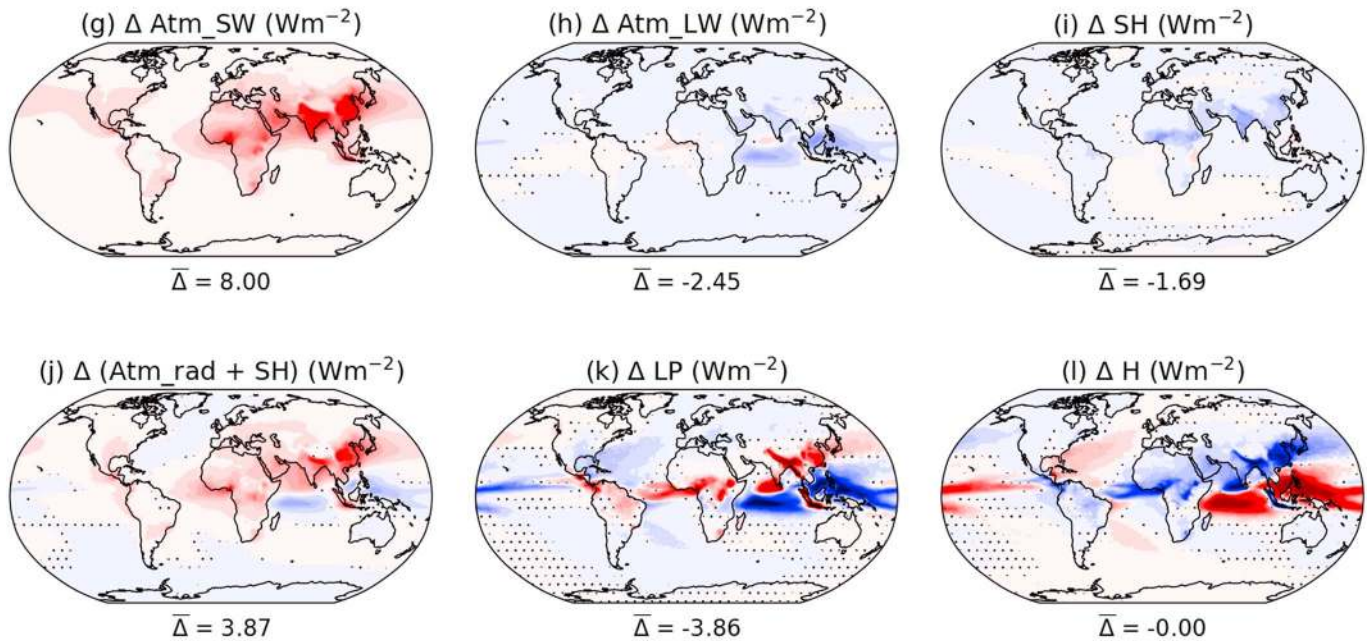


**Figure 7.** Impacts of 10xBC on the multiannual mean atmospheric energy budget components in the free-running experiment. Plots show changes to (a, g) short-wave radiative absorption (Atm\_SW), (b, h) longwave radiative absorption (Atm\_LW), (c, i) surface latent heat (SH), (d, j) the sum of radiative and sensible heat (Atm\_rad + SH, referred to as “Q” in other publications), (e, k) latent heat release from precipitation (LP), and (f, l) the dynamical heat convergence (H) calculated as the residual of  $Q - LP$ . Stipples indicate regions where changes are not statistically significant at the 80% confidence level.

Increased SW heating from BC must therefore be rebalanced through a combination of increased LW cooling and downward adjustments in SH and LP (Ming et al., 2010; Smith et al., 2018). The 10xBC perturbation in these experiments increased global-mean solar absorption in the atmosphere by  $8.4 \text{ W/m}^2$  ( $8.0 \text{ W/m}^2$ ) in the free-running (nudged) experiment. Regionally, the SW absorption was strongest over Tropical Asia and Africa (Figures 7a and 7g) where BC mass loadings were high and solar insolation was relatively strong. LW emission (radiative cooling) in the atmosphere increased globally by  $2.7 \text{ W/m}^2$  ( $2.4 \text{ W/m}^2$ ) in the free-running (nudged) experiment due to the combined effects of increases in atmospheric temperature and changes in cloud and water vapor. The surface sensible heat flux (SH) reduced by  $1.7 \text{ W/m}^2$  in both experiments, with the strongest local reductions over Tropical Africa and Asia due to decreased surface insolation and reduced surface temperature (Figures S3a and S3b). The resulting change in atmospheric heating ( $\Delta Q$ ) from changes in radiation and surface sensible heat fluxes ( $\Delta Q = \Delta \text{Atm\_SW} + \Delta \text{Atm\_LW} + \Delta \text{SH}$ ; Figures 7d and 7j) was  $3.9 \text{ W/m}^2$ , and this was exactly balanced by reduced latent heat from precipitation ( $\Delta \text{LP}$ ); see Figures 7e and 7k. This global-scale balance holds in both experiments, and it is clear from the comparison between the two experiments that BC-driven changes in atmospheric circulation do not have much influence on these global-scale adjustments to the energy budget.

On regional scales, perturbations to atmospheric heating ( $\Delta Q$ ) are not balanced by  $\Delta \text{LP}$ ; in fact, strong heating over Tropical Asia and Africa (Figures 7d and 7j) locally enhances convective precipitation (Figures 7e and 7k) adding to the atmospheric heating. Reductions in precipitation occur elsewhere where the atmospheric heating is smaller or negative. This feedback leads to even larger local changes in atmospheric heating that are balanced by changes in heat transport ( $\Delta H$ ) from thermal advection. In this study, changes in heat transport were derived as a residual assuming that the global multiannual mean heat content of the atmosphere does not change with time ( $\Delta H + \Delta \text{LP} + \Delta Q = 0$ ). As shown in Richardson et al. (2018), the H term is typically dominated by changes in vertical motion, especially in the tropics. As potential temperature generally increases with height, ascent generally causes dynamical cooling, and vice versa for descent. This explains the high degree of anticorrelation between  $\Delta \text{LP}$  and  $\Delta H$  (Figures 7e–7f and 7k–7l and Table S2) and the correlation of  $\Delta H$  with vertical velocity changes (Figures 4a and 4b and Table S2). This balance between changes in latent heating and dynamical warming/cooling (Figures 7e–7f and 7k–7l) also seems to dominate the regional heat budget in the midlatitudes. Vertical motion decreases over the storm track regions, particularly in the NH, and this likely explains the dynamical warming in those regions (Figures 7f and 7l). A further contribution may come from reduced horizontal transports associated with planetary waves and/or eddies, but this cannot be deduced from the present analysis.

In summary, the analysis of Figure 7 shows that changes in atmospheric circulation are not important in explaining how the atmosphere's heat budget adjusts to BC on a global scale. At regional scales, however, changes in vertical motion play a key role in balancing out changes in radiative heating and precipitation. As the nudged experiment permitted some changes to vertical motion, particularly in the tropics, these regional adjustments have been illustrated, to some degree, in both experiments.

#### 4. Conclusions and Discussion

This study investigated whether changes in atmospheric circulation were important in governing how clouds, precipitation, and the radiation budget rapidly adjust to forcing by BC aerosol. This question has been answered by contrasting results from a standard (free-running) fixed SST experiment against a parallel experiment where the horizontal winds were nudged toward meteorological reanalyses. In both experiments, present-day BC emissions were increased by a factor of 10 while keeping SSTs fixed, to allow an analysis of the RA in the atmosphere-land system. The results show that changes in the large-scale atmospheric circulation are not crucial in determining RA to the global-mean radiation budget or global precipitation. At the global scale, these adjustments are driven by changes in convection and cloud cover linked to increased radiative heating and static stability in the atmosphere. These adjustments are captured reasonably well even when the atmospheric flow is nudged, provided that temperatures are not nudged. On the other hand, changes in atmospheric circulation were important in determining regional impacts of BC on precipitation and clouds.

The 10xBC perturbation led to an ERF of  $2.70 \text{ W/m}^2$  in the free-running experiment and  $2.77 \text{ W/m}^2$  in the nudged experiment. These ERFs were almost equal to the IRF, as although RA in clouds led to strong

changes in SW and LW radiation (particularly at regional scales), these cancelled out to have virtually zero impact on global-mean net TOA radiation. This result differs from previous studies that concluded BC RA to be overall negative. In our model, negative LW adjustments due to reduced high cloud (linked to the suppression of deep convection) approximately balanced positive SW adjustments due to an overall reduction of cloud cover (despite increases in stratocumulus over the oceans). The global-mean results were approximately the same in the nudged experiment, even though the regional patterns of SW and LW adjustments were somewhat different. Changes in atmospheric circulation therefore do not seem to be crucial in determining the ERF of BC aerosol. This indicates that preliminary estimates of aerosol ERF can be provided from nudged simulations, even for highly absorbing aerosol. This further supports the findings of Forster et al. (2016) where ERF estimates for a range of climate forcings were comparable in nudged and free-running fixed SST experiments. The result also helps to justify the use of nudging when testing improvements to aerosols in global models (e.g., Mollard, 2017) or exploring how parametric uncertainty affects ERFs (e.g., Regayre et al., 2018). Furthermore, it suggests that differences in dynamical responses are unlikely to be the major reason for the current disagreement among models on whether BC forcing is weakened by negative RA.

BC absorption reduced global precipitation by around 0.13 mm/day in both the free-running and nudged experiments. This was associated with reductions in deep convection and was consistent with the increase in radiative absorption that reduces demand for latent heat release in the atmosphere. This requirement for energy balance in the global atmosphere still held in the nudged experiment, and this result shows that the global precipitation response to BC is not particularly sensitive to the evolution of dynamical feedbacks. However, at regional scales, BC heating led to large changes in precipitation (both positive and negative), cloud, and convective activity, and these impacts were strongly linked to changes in atmospheric circulation.

In the tropics, regional impacts on cloud and precipitation were linked to feedback between BC heating, vertical motion, and deep convection. This dynamical feedback enhanced precipitation over Tropical Asia and Africa by up to 750–1,500 mm/day. Compensating descent suppressed convection over surrounding tropical oceans, especially the Indian Ocean and West Pacific. These impacts were just as strong in the nudged experiment, but the associated changes in vertical motion were supported by relatively small adjustments in the divergent component of the flow that nudging did not prevent. Changes in the Walker circulation (zonal flow) were suppressed by the nudging, and this meant that the regions of compensating drying/descent were less widespread than those in the free-running experiment.

In the midlatitudes, changes in atmospheric flow were of key importance in determining the RA of clouds and precipitation to BC. The main impacts were a large reduction in middle- and high-level clouds and precipitation in the NH midlatitude storm tracks. This was associated with a poleward shift of upper-level jets and weakening of associated surface weather patterns. The reasons for this shift are complex but likely stem from strong heating in the NH subtropics and midlatitudes that reduces the demand for poleward heat transport in the atmosphere and alters meridional temperature gradients (and the associated baroclinic instability). These dynamical responses were inhibited by the nudging, limiting the associated impacts on clouds, precipitation, and radiation.

BC generally increased low cloud cover over the oceans, due to increased LTS. This negative semidirect effect response was exhibited in both experiments, but the increases in marine low cloud were more pronounced in the free-running experiment, particularly in the NH subtropics. This was linked to changes in large-scale flow (subsidence) that further increased LTS.

In summary, the study has shown that changes in atmospheric circulation have a mixed role in shaping how BC affects clouds, precipitation, and the radiation budget. While global-mean impacts do not seem sensitive to circulation changes, dynamical responses have a key role in most regional impacts, particularly in shaping where precipitation changes occur.

One further point to note is that similar regional patterns of precipitation change also emerge in  $2xCO_2$  fixed-SST experiments (e.g., Chadwick et al., 2019; Richardson et al., 2018), even though the atmospheric forcing from  $CO_2$  is far more uniform than that from BC. Results from a companion  $2xCO_2$  experiment are shown in the supporting information (Figure S6) and illustrate that although the RA in cloud, precipitation, and atmospheric circulation are much weaker for  $2xCO_2$  than for  $10xBC$ , many of the spatial patterns are similar. Regional impacts from BC are therefore not necessarily unique to the spatial concentration of BC



forcing. These may be somewhat generic responses to increased radiative absorption and/or preferential warming over continents (in fixed SST experiments). These responses may depend more on the baseline simulation of atmospheric circulation in the climate model. This may be one reason that regional impacts of BC on precipitation and cloud vary considerably among state-of-the-art general circulation models. However, we conclude that differing dynamical responses are unlikely to explain the intermodel diversity in BC ERF estimates. Further analysis of RA and dynamical responses in multimodel experiments would be useful to test this conclusion.

#### Acknowledgments

Ben Johnson and Jim Haywood were funded under the joint UK BEIS/DEFRA–Met Office Hadley Centre Climate Programme (GA01101). M. H. was supported by the Natural Environment Research Council (NERC)/Department for International Development via the Future Climates for Africa (FCFA)-funded project “Improving Model Processes for African Climate” (IMPALA, NE/M017265/1). Data from the model experiments are archived and available online from <https://doi.org/10.5281/zenodo.2579637>. Finally, we are grateful for constructive input and discussion from Christine Johnson, Duncan Ackerley, Ruth McDonald, Robin Chadwick, Piers Forster, Chris Smith, and Tom Richardson.

#### References

- Ackerman, A. S., Toon, O. B., Stevens, D. E., Heymsfield, A. J., Ramanathan, V., & Welton, E. J. (2000). Reduction of tropical cloudiness by soot. *Science*, *288*(5468), 1042–1047. <https://doi.org/10.1126/science.288.5468.1042>
- Allen, R. J., & Sherwood, S. C. (2010). Aerosol–cloud semi-direct effect and land–sea temperature contrast in a GCM. *Geophysical Research Letters*, *37*, L07702. <https://doi.org/10.1029/2010GL042759>
- Allen, R. J., Sherwood, S. C., Norris, J. R., & Zender, C. S. (2012). Recent Northern Hemisphere tropical expansion primarily driven by black carbon and tropospheric ozone. *Nature*, *485*(7398), 350–354. <https://doi.org/10.1038/nature11097>
- Andreae, M. O., & Ramanathan, V. (2013). Climate’s dark forcings. *Science*, *340*(6130), 280–281. <https://doi.org/10.1126/science.1235731>
- Andrews, T., Forster, P. M., Boucher, O., Bellouin, N., & Jones, A. (2010). Precipitation radiative forcing and global temperature change. *Geophysical Research Letters*, *37*, L14701. <https://doi.org/10.1029/2010GL043991>
- Baker, L. H., Collins, W. J., Ollivié, D. J. L., Cherian, R., Hodnebrog, Ø., Myhre, G., & Quaas, J. (2015). Climate responses to anthropogenic emissions of short-lived climate pollutants. *Atmospheric Chemistry and Physics*, *15*(14), 8201–8216. <https://doi.org/10.5194/acp-15-8201-2015>
- Bond, T. C., Doherty, S. J., Fahey, D. W., Forster, P. M., Berntsen, T., DeAngelo, B. J., et al. (2013). Bounding the role of black carbon in the climate system: A scientific assessment. *Journal of Geophysical Research: Atmospheres*, *118*, 5380–5552. <https://doi.org/10.1002/jgrd.50171>
- Boucher, O., Balkanski, Y., Hodnebrog, Ø., Lund Myhre, C., Myhre, G., Quaas, J., et al. (2016). Jury is still out on the radiative forcing by black carbon. *Proceedings of the National Academy of Sciences of the United States of America*, *113*(35), E5092–E5093. <https://doi.org/10.1073/pnas.1607005113>
- Boucher, O., Randall, D., Artaxo, P., Bretherton, C., Feingold, G., Forster, P., et al. (2013). The physical science basis. Contribution of Working Group I to the Fifth Assessment Report of the Intergovernmental Panel on Climate Change. In T. F. Stocker, D. Qin, G.-K. Plattner, M. Tignor, S. K. Allen, J. Boschung, A. Nauels, Y. Xia, V. Bex, & P. M. Midgley (Eds.), *Clouds and aerosols, in: Climate Change*, (pp. 571–657). Cambridge, UK and New York, NY, USA: Cambridge University Press.
- Chadwick, R., Ackerley, D., Ogura, T., & Dommengat, D. (2019). Separating the influences of land warming, the direct CO<sub>2</sub> effect, the plant physiological effect, and SST warming on regional precipitation changes. *Journal of Geophysical Research: Atmospheres*, *124*, 624–640. <https://doi.org/10.1029/2018JD029423>
- Chadwick, R., Boutle, I., & Martin, G. (2013). Spatial patterns of precipitation change in CMIP5: Why the rich do not get richer in the tropics. *Journal of Climate*, *26*, 3803–3822. <https://doi.org/10.1175/JCLI-D-12-00543.1>
- Chung, C. E., Ramanathan, V., & Decremier, D. (2012). Observationally constrained estimates of carbonaceous aerosol radiative forcing. *Proceedings of the National Academy of Sciences of the United States of America*, *109*(29), 11,624–11,629. <https://doi.org/10.1073/pnas.1203707109>
- Dai, A. (2006). Precipitation characteristics in eighteen coupled climate models. *Journal of Climate*, *19*, 4605–4630. <https://doi.org/10.1175/JCLI3884.1>
- Dee, D. P., Uppala, S. M., Simmons, A. J., Berrisford, P., Poli, P., Kobayashi, S., et al. (2011). The ERA-interim reanalysis: Configuration and performance of the data assimilation system. *Quarterly Journal of the Royal Meteorological Society*, *137*(656), 553–597. <https://doi.org/10.1002/qj.828>
- Fan, J., Rosenfeld, D., Yang, Y., Zhao, C., Leung, L. R., & Li, Z. (2015). Substantial contribution of anthropogenic air pollution to catastrophic floods in Southwest China. *Geophysical Research Letters*, *42*, 6066–6075. <https://doi.org/10.1002/2015GL064479>
- Forster, P. M., Richardson, T., Maycock, A. C., Smith, C. J., Samset, B. H., Myhre, G., et al. (2016). Recommendations for diagnosing effective radiative forcing from climate models for CMIP6. *Journal of Geophysical Research: Atmospheres*, *121*, 12,460–12,475. <https://doi.org/10.1002/2016JD025320>
- Frieler, K., Meinshausen, M., von Deimling, T. S., Andrews, T., & Forster, P. (2011). Changes in global-mean precipitation in response to warming, greenhouse gas forcing and black carbon. *Geophysical Research Letters*, *38*, L04702. <https://doi.org/10.1029/2010GL045953>
- Ghan, S., Wang, M., Zhang, S., Ferrachat, S., Gettelman, A., Griesfeller, J., et al. (2016). Challenges in constraining anthropogenic aerosol effects on cloud radiative forcing using present-day spatiotemporal variability. *Proceedings of the National Academy of Sciences*, *113*(21), 5804–5811. <https://doi.org/10.1073/pnas.1514036113>
- Ghan, S. J., Liu, X., Easter, R. C., Zaveri, R., Rasch, P. J., Yoon, J., & Eaton, B. (2012). Toward a minimal representation of aerosols in climate models: Comparative decomposition of aerosol direct, semidirect, and indirect radiative forcing. *Journal of Climate*, *25*, 6461–6476. <https://doi.org/10.1175/JCLI-D-11-00650.1>
- Hansen, J., Sato, M., & Ruedy, R. (1997). Radiative forcing and climate response. *Journal of Geophysical Research*, *102*(D6), 6831–6864. <https://doi.org/10.1029/96JD03436>
- Hoelsy, R. M., Smith, S. J., Feng, L., Klimont, Z., Janssens-Maenhout, G., Pitkanen, T., et al. (2018). Historical (1750–2014) anthropogenic emissions of reactive gases and aerosols from the Community Emissions Data System (CEDS). *Geoscientific Model Development*, *11*(1), 369–408. <https://doi.org/10.5194/gmd-11-369-2018>
- Jacobson, M. Z. (2001). Strong radiative heating due to the mixing state of black carbon in atmospheric aerosols. *Nature*, *409*(6821), 695–697. <https://doi.org/10.1038/3505518>
- Johnson, B. T. (2005). The semidirect aerosol effect: Comparison of a single-column model with large eddy simulation for marine stratocumulus. *Journal of Climate*, *18*(1), 119–130. <https://doi.org/10.1175/JCLI-3233.1>
- Johnson, B. T., Shine, K. P., & Forster, P. M. (2004). The semi-direct aerosol effect: Impact of absorbing aerosols on marine stratocumulus. *Quarterly Journal of the Royal Meteorological Society*, *130*(599), 1407–1422. <https://doi.org/10.1256/qj.03.61>



- Kipling, Z., Stier, P., Schwarz, J. P., Perring, A. E., Spackman, J. R., Mann, G. W., et al. (2013). Constraints on aerosol processes in climate models from vertically-resolved aircraft observations of black carbon. *Atmospheric Chemistry and Physics*, *13*(12), 5969–5986. <https://doi.org/10.5194/acp-13-5969-2013>
- Koch, D., Balkanski, Y., Bauer, S. E., Easter, R. C., Ferrachat, S., Ghan, S. J., et al. (2011). Soot microphysical effects on liquid clouds, a multi-model investigation. *Atmospheric Chemistry and Physics*, *11*(3), 1051–1064. <https://doi.org/10.5194/acp-11-1051-2011>
- Koch, D., & Del Genio, A. D. (2010). Black carbon semi-direct effects on cloud cover: Review and synthesis. *Atmospheric Chemistry and Physics*, *10*(16), 7685–7696. <https://doi.org/10.5194/acp-10-7685-2010>
- Koch, D., Schulz, M., Kinne, S., McNaughton, C., Spackman, J. R., Balkanski, Y., et al. (2009). Evaluation of black carbon estimations in global aerosol models. *Atmospheric Chemistry and Physics*, *9*(22), 9001–9026. <https://doi.org/10.5194/acp-9-9001-2009>
- Kooperman, G. J., Pritchard, M. S., Ghan, S. J., Wang, M., Somerville, R. C. J., & Russell, L. M. (2012). Constraining the influence of natural variability to improve estimates of global aerosol indirect effects in a nudged version of the Community Atmosphere Model 5. *Journal of Geophysical Research*, *117*, D23204. <https://doi.org/10.1029/2012JD018588>
- Kovilakam, M., & Mahajan, S. (2015). Black carbon aerosol-induced Northern Hemisphere tropical expansion. *Geophysical Research Letters*, *42*, 4964–4972. <https://doi.org/10.1002/2015GL064559>
- Lau, K.-M., & Kim, K.-M. (2006). Observational relationships between aerosol and Asian monsoon rainfall, and circulation. *Geophysical Research Letters*, *33*, L21810. <https://doi.org/10.1029/2006GL027546>
- Lin, Y., Wang, Y., Pan, B., Hu, J., Liu, Y., & Zhang, R. (2016). Distinct impacts of aerosols on an evolving continental cloud complex during the RACORO field campaign. *Journal of the Atmospheric Sciences*, *73*(9), 3681–3700. <https://doi.org/10.1175/JAS-D-15-0361.1>
- Liu, L., Shawki, D., Voulgarakis, A., Kasoar, M., Samset, B. H., Myhre, G., et al. (2018). A PDRMIP multimodel study on the impacts of regional aerosol forcings on global and regional precipitation. *Journal of Climate*, *31*, 4429–4447. <https://doi.org/10.1175/JCLI-D-17-0439.1>
- Mann, G. W., Carslaw, K. S., Spracklen, D. V., Ridley, D. A., Manktelow, P. T., Chipperfield, M. P., et al. (2010). Description and evaluation of GLOMAP-mode: a modal global aerosol microphysics model for the UKCA composition-climate model. *Geoscientific Model Development*, *3*(2), 519–551. <https://doi.org/10.5194/gmd-3-519-2010>
- Mahajan, S., Evans, K. J., Hack, J. J., & Truesdale, J. E. (2013). Linearity of climate response to increases in black carbon aerosols. *Journal of Climate*, *26*, 8223–8237. <https://doi.org/10.1175/JCLI-D-12-00715.1>
- Malavelle, F., Haywood, J. M., Jones, A., Gettelman, A., Clarisse, L., Bauduin, S., et al. (2017). Strong constraints on aerosol–cloud interactions from volcanic eruptions. *Nature*, *546*(7659), 485–491. <https://doi.org/10.1038/nature22974>
- Matsui, H., Hamilton, D., & Mahowald, N. M. (2018). Black carbon radiative effects highly sensitive to emitted particle size when resolving mixing-state diversity. *Nature Communications*, *9*(1), 3446. <https://doi.org/10.1038/s41467-018-05635-1>
- Meehl, G. A., Arblaster, J. M., & Collins, W. D. (2008). Effects of black carbon aerosols on the Indian monsoon. *Journal of Climate*, *21*, 2869–2882. <https://doi.org/10.1175/2007JCLI1777.1>
- Menon, S., Hansen, J. E., Nazarenko, L., & Luo, Y. (2002). Climate effects of black carbon aerosols in China and India. *Science*, *297*(5590), 2250–2253. <https://doi.org/10.1126/science.1075159>
- Ming, Y., Ramaswamy, V., & Persad, G. (2010). Two opposing effects of absorbing aerosols on global-mean precipitation. *Geophysical Research Letters*, *37*, L13701. <https://doi.org/10.1029/2010GL042895>
- Mollard, J. (2017). Improving the simulation of carbonaceous aerosol in HadGEM3-UKCA, Phd thesis, University of Reading Dept. Meteorol., [http://centaur.reading.ac.uk/75678/1/18001810\\_Mollard\\_thesis.pdf](http://centaur.reading.ac.uk/75678/1/18001810_Mollard_thesis.pdf).
- Morgenstern, O., Braesicke, P., O'Connor, F. M., Bushell, A. C., Johnson, C. E., Osprey, S. M., & Pyle, J. A. (2009). Evaluation of the new UKCA climate-composition model—Part 1: The stratosphere. *Geoscientific Model Development*, *2*, 43–57. <https://doi.org/10.5194/gmd-2-43-2009>
- Mulcahy, J. P., Jones, C., Sellar, A., Johnson, B., Boutle, I. A., Jones, A., et al. (2018). Improved aerosol processes and effective radiative forcing in HadGEM3 and UKESM1. *Journal of Advances in Modeling Earth Systems*, *10*, 2786–2805. <https://doi.org/10.1029/2018MS001464>
- Myhre, G., Forster, P. M., Samset, B. H., Hodnebrog, Ø., Sillmann, J., Aalbergsjø, S. G., et al. (2017). PDRMIP: A precipitation driver and response model intercomparison project—Protocol and preliminary results. *Bulletin of the American Meteorological Society*, *98*(6), 1185–1198. <https://doi.org/10.1175/BAMS-D-16-0019.1>
- Myhre, G., Kramer, R. J., Smith, C. J., Hodnebrog, Ø., Forster, P., Soden, B. J., et al. (2018). Quantifying the importance of rapid adjustments for global precipitation changes. *Geophysical Research Letters*, *45*, 11,399–11,405. <https://doi.org/10.1029/2018GL079474>
- Myhre, G., Samset, B. H., Schulz, M., Balkanski, Y., Bauer, S., Bernsten, T. K., et al. (2013). Radiative forcing of the direct aerosol effect from AeroCom Phase II simulations. *Atmospheric Chemistry and Physics*, *13*, 1853–1877. <https://doi.org/10.5194/acp-13-1853-2013>
- O'Connor, F. M., Johnson, C. E., Morgenstern, O., Abraham, N. L., Braesicke, P., Dalvi, M., et al. (2014). Evaluation of the new UKCA climate-composition model—Part 2: The troposphere. *Geoscientific Model Development*, *7*(1), 41–91. <https://doi.org/10.5194/gmd-7-41-2014>
- Peng, J. (2016). Markedly enhanced absorption and direct radiative forcing of black carbon under polluted urban environments. *Proceedings of the National Academy of Sciences*, *113*(16), 4266–4271. <https://doi.org/10.1073/pnas.1602310113>
- Ramanathan, V., & Carmichael, G. (2008). Global and regional climate changes due to black carbon. *Nature Geoscience*, *1*(4), 221–227. <https://doi.org/10.1038/ngeo156>
- Regayre, L. A., Johnson, J. S., Yoshioka, M., Pringle, K. J., Sexton, D. M. H., Booth, B. B. B., et al. (2018). Aerosol and physical atmosphere model parameters are both important sources of uncertainty in aerosol ERF. *Atmospheric Chemistry and Physics*, *18*(13), 9975–10006. <https://doi.org/10.5194/acp-18-9975-2018>
- Reynolds, R. W., Smith, T. M., Liu, C., Chelton, D. B., Casey, K. S., & Schlax, M. G. (2007). Daily high-resolution-blended analyses for sea surface temperature. *Journal of Climate*, *20*, 5473–5496. <https://doi.org/10.1175/2007JCLI1824.1>
- Richardson, T. B., Forster, P. M., Andrews, T., Boucher, O., Faluvegi, G., Fläschner, D., et al. (2018). Drivers of precipitation change: An energetic understanding. *Journal of Climate*, *31*, 9641–9657. <https://doi.org/10.1175/JCLI-D-17-0240.1>
- Roberts, D. L., & Jones, A. (2004). Climate sensitivity to black carbon aerosol from fossil fuel combustion. *Journal of Geophysical Research*, *109*, D16202. <https://doi.org/10.1029/2004JD004676>
- Samset, B. H., & Myhre, G. (2015). Climate response to externally mixed black carbon as a function of altitude. *Journal of Geophysical Research: Atmospheres*, *120*, 2913–2927. <https://doi.org/10.1002/2014JD022849>

- Samset, B. H., Myhre, G., Forster, P. M., Hodnebrog, Ø., Andrews, T., Faluvegi, G., et al. (2016). Fast and slow precipitation responses to individual climate forcings: A PDRMIP multimodel study. *Geophysical Research Letters*, *43*, 2782–2791. <https://doi.org/10.1002/2016GL068064>
- Samset, B. H., Myhre, G., Schulz, M., Balkanski, Y., Bauer, S., Bernsten, T. K., et al. (2013). Black carbon vertical profiles strongly affect its radiative forcing uncertainty. *Atmospheric Chemistry and Physics*, *13*(5), 2423–2434. <https://doi.org/10.5194/acp-13-2423-2013>
- Samset, B. H., Stjern, C. W., Andrews, E., Kahn, R., Myhre, G., Schulz, M., & Schuster, G. (2018). Aerosol absorption: Progress towards global and regional constraints. *Current Climate Change Reports*, *4*, 65–83. <https://doi.org/10.1007/s40641-018-0091-4>
- Sand, M., Iversen, T., Böhlinger, P., Kirkevåg, A., Seierstad, I., Seland, Ø., & Sorteberg, A. (2015). A standardized global climate model study showing unique properties for the climate response to black carbon aerosols. *Journal of Climate*, *28*, 2512–2526. <https://doi.org/10.1175/JCLI-D-14-00050.1>
- Sato, M., Hansen, J., Koch, D., Lacis, A., Ruedy, R., Dubovik, O., et al. (2003). Global atmospheric black carbon inferred from AERONET. *Proceedings of the National Academy of Sciences of the United States of America*, *100*(11), 6319–6324. <https://doi.org/10.1073/pnas.0731897100>
- Smith, C. J., Kramer, R. J., Myhre, G., Forster, P. M., Soden, B. J., Andrews, T., et al. (2018). Understanding rapid adjustments to diverse forcing agents. *Geophysical Research Letters*, *45*, 12,023–12,031. <https://doi.org/10.1029/2018GL079826>
- Stjern, C. W., Samset, B. H., Myhre, G., Forster, P. M., Hodnebrog, Ø., Andrews, T., & Voulgarakis, A. (2017). Rapid adjustments cause weak surface temperature response to increased black carbon concentrations. *Journal of Geophysical Research: Atmospheres*, *122*, 11,462–11,481. <https://doi.org/10.1002/2017JD027326>
- Tang, T., Shindell, D., Samset, B. H., Boucher, O., Forster, P. M., Hodnebrog, Ø., et al. (2018). Dynamical response of Mediterranean precipitation to greenhouse gases and aerosols. *Atmospheric Chemistry and Physics*, *18*(11), 8439–8452. <https://doi.org/10.5194/acp-18-8439-2018>
- Telford, P. J., Braesicke, P., Morgenstern, O., & Pyle, J. A. (2008). Technical note: Description and assessment of a nudged version of the new dynamics Unified Model. *Atmospheric Chemistry and Physics*, *8*(6), 1701–1712. <https://doi.org/10.5194/acp-8-1701-2008>
- Walters, D., Baran, A. J., Boutle, I., Brooks, M., Earnshaw, P., Edwards, J., et al. (2019). The Met Office Unified Model Global Atmosphere 7.0/7.1 and JULES Global Land 7.0 configurations. *Geoscientific Model Development*, *12*(5), 1909–1963. <https://doi.org/10.5194/gmd-12-1909-2019>
- Wang, C. (2004). A modeling study on the climate impacts of black carbon aerosols. *Journal of Geophysical Research*, *109*, D03106. <https://doi.org/10.1029/2003JD004084>
- Wang, C. (2009). The sensitivity of tropical convective precipitation to the direct radiative forcings of black carbon aerosols emitted from major regions. *Annales Geophysicae*, *27*(10), 3705–3711. <https://doi.org/10.5194/angeo-27-3705-2009>
- Wang, C. (2013b). Impact of anthropogenic absorbing aerosols on clouds and precipitation (2012), A review of recent progresses. *Atmospheric Environment*, *122*, 237–249. <https://doi.org/10.1016/j.atmosres.2012.11.005>
- Wang, Q., Jacob, D. J., Spackman, J. R., Perring, A. E., Schwarz, J. P., Moteki, N., et al. (2014). Global budget and radiative forcing of black carbon aerosol: Constraints from pole-to-pole (HIPPO) observations across the Pacific. *Journal of Geophysical Research: Atmospheres*, *119*, 195–206. <https://doi.org/10.1002/2013JD020824>
- Wang, R., Balkanski, Y., Boucher, O., Ciais, P., Schuster, G. L., Chevallier, F., et al. (2016). Estimation of global black carbon direct radiative forcing and its uncertainty constrained by observations. *Journal of Geophysical Research: Atmospheres*, *121*, 5948–5971. <https://doi.org/10.1002/2015JD024326>
- Wang, Y. (2013a). New directions: Light absorbing aerosols and their atmospheric impacts. *Atmospheric Environment*, *81*, 713–715. <https://doi.org/10.1016/j.atmosenv.2013.09.034>
- Wilcox, E. M. (2010). Stratocumulus cloud thickening beneath layers of absorbing smoke aerosol. *Atmospheric Chemistry and Physics*, *10*, 11,769–11,777. <https://doi.org/10.5194/acp-10-11769-2010>
- Yoshimori, M., & Broccoli, A. J. (2008). Equilibrium response of an atmosphere–mixed layer ocean model to different radiative forcing agents: Global and zonal mean response. *Journal of Climate*, *21*, 4399–4423. <https://doi.org/10.1175/2008JCLI2172.1>
- Zarzycki, C. M., & Bond, T. C. (2010). How much can the vertical distribution of black carbon affect its global direct radiative forcing? *Geophysical Research Letters*, *37*, L20807. <https://doi.org/10.1029/2010GL044555>
- Zhang, H., & Wang, Z. (2011). Advances in the study of black carbon effects on climate. *Advances in Climate Change Research*, *2*(1), 23–30. <https://doi.org/10.3724/SP.J.1248.2011.00023>
- Zhang, K., Wan, H., Liu, X., Ghan, S. J., Kooperman, G. J., Ma, P.-L., et al. (2014). Technical Note: On the use of nudging for aerosol–climate model intercomparison studies. *Atmospheric Chemistry and Physics*, *14*, 8631–8645. <https://doi.org/10.5194/acp-14-8631-2014>